

Listening to the Universe with Next Generation Ground-Based Gravitational-Wave Detectors

Ssohrab Borhanian¹ and B. S. Sathyaprakash^{1,2,3}

¹*Institute for Gravitation and the Cosmos, Department of Physics, Pennsylvania State University, University Park, PA 16802, USA*

²*Department of Astronomy and Astrophysics, Pennsylvania State University, University Park, PA 16802, USA*

³*School of Physics and Astronomy, Cardiff University, Cardiff, CF24 3AA, United Kingdom*

(Dated: June 2, 2021)

Discoveries made by the Laser Interferometer Gravitational-Wave Observatory (LIGO) and Virgo have ushered in the era of gravitational-wave astronomy. Upgrades in instrumentation and technology over the next five to ten years will enable these detectors to explore sources with higher fidelity with the potential to make phenomenal new discoveries. To realize its full potential gravitational-wave astronomy would require the construction of new facilities that can host increasingly improved instrumentation for a period of ~ 50 years. In this paper, we use simple performance metrics to assess the science capabilities of planned and future networks. These metrics all refer to coalescences of binary neutron stars and black holes and include: (i) network detection efficiency and detection rate of cosmological sources and their number densities as a function of redshift, (ii) signal-to-noise ratios and the accuracy with which intrinsic and extrinsic parameters would be measured, and (iii) enabling multimessenger astronomy with gravitational waves by accurate 3D localization and early warning alerts. We will in addition discuss the science enabled by the small population of loud and rare events. While imminent upgrades will provide impressive advances in all these metrics, future observatories of Cosmic Explorer and Einstein Telescope, currently being planned, will realize the full potential of gravitational-wave astronomy over the next two to three decades—observing coalescing compact binaries from epochs before the formation of first stars, should they exist.

I. INTRODUCTION:

A. Dawn of gravitational-wave astronomy

Over the past five years and three observing runs, the Advanced Laser Interferometer Gravitational-Wave Observatory (LIGO) consisting of the LIGO-Hanford and LIGO-Livingston detectors [1] and the Virgo detector [2] have discovered gravitational waves (GWs) from the merger of dozens of binary black holes (BBHs) [3–7], two binary neutron stars (BNSs) [8, 9] and a candidate binary neutron star-black hole [7]. In addition to the pioneering first direct observation of GWs from a pair of merging BBHs (GW150914) [3], LIGO and Virgo have made many spectacular and surprising new discoveries. These include amongst others a BNS merger that was observed in the entire electromagnetic window from gamma-rays to radio waves (GW170817) [8, 10, 11], systems in which black hole (BH) companions have masses larger than anyone expected, thus raising questions as to their origin (GW170729 [12] and GW190521 [13, 14]), binaries that show a clear signature of sub-dominant octupole radiation in addition to the dominant quadrupole, confirming once again predictions of general relativity (GW190412 [15] and GW190814 [16]), and a binary with a mass-ratio of almost 1:10 that challenges astrophysical BBH formation models while its secondary companion could well be the heaviest neutron star (NS) or the lightest BH observed so far (GW190814 [16]).

These discoveries have already made a massive impact on our understanding of different tenets of astrophysics, fundamental physics and cosmology. They have allowed a first glimpse into the dynamics of strongly curved spacetimes and the validity of general relativity in unexplored regimes of the theory [17–19], raised deeper questions on the formation mechanisms and evolutionary scenarios of compact objects [14, 16, 20], provided a new tool for measuring cosmic distances that will help in precision cosmology [21, 22] and in mapping the large scale structure of the Universe, brought to bear a novel ap-

proach to determine the structure and properties of NSs to help in the exploration of the dense matter equation of state which governs the dynamics of NS cores [23–25].

At the same time, multimessenger observations of GW170817—the inspiral and coalescence of a pair of NSs—have at once begun to impact on several enigmatic questions in nuclear astrophysics and fundamental physics. We now know that BNS mergers are progenitors of short, hard gamma-ray bursts [11] and sites where r-process heavy elements are produced from neutron-rich ejecta [26–35], GWs essentially travel at the speed of light [11], which has helped rule out certain alternative theories of gravity that were invoked to explain the origin of dark energy [36], and that the dense matter equation of state cannot be too stiff, thus constraining the radius of NSs of $1.4 M_{\odot}$ to be below about 14 km [24, 25].

LIGO-Virgo discoveries have led to numerous investigations about the properties of NSs and BHs including the maximum mass of NSs [37–41], potential primordial origin of the observed BHs [42–44], stochastic backgrounds that might be produced by the astrophysical population of BBH and BNS mergers [45–47] to name a few. It has already become clear that the GW window has the potential to transform our knowledge of physics and astronomy in the coming decades—some of which we hope to explore in this study.

B. Imminent upgrade and new detectors

With significant improvements in sensitivity expected over the next five years (A+ detector generation) [48, 49] and the addition of two new detectors, KAGRA [50, 51]. The Hubble-Lemaître tension—the discrepancy between the early and late Universe measurements of the Hubble constant [52]—could be resolved with multimessenger observations of ~ 50 BNS mergers [53] or with the identification of a handful of BBHs within 500 Mpc [54]. We will explore in detail the potential of this imminent A+ detector generation, using the A+, V+, and

K+ noise curves shown in Fig. 1.

C. Future of gravitational-wave astronomy

It is possible to further enhance the sensitivity of current facilities with new laser, cryo-cooled mirror substrates, active noise cancellation techniques for gravity gradient and the like. The concept of Voyager technology [55], which can be installed in current facilities, aims to improve the sensitivity beyond A+ detectors by a factor of ~ 2 to 4 depending on the frequency. New facilities and instrumentation would be needed to make sensitivity improvements beyond that facilitated by the Voyager concept. Einstein Telescope (ET) [56, 57], Cosmic Explorer (CE) [58] and Neutron Star Extreme Matter Observatory (NEMO) [59] are three such concepts (jointly referred to as third-generation or, simply, 3G) that are currently being pursued with the hope of first facilities being built within the next 10 to 15 years.

There have been extensive studies on the capability of next generation of detectors and the scientific discoveries they enable [60–72]. The Voyager network would localize ~ 160 BNS mergers within 500 Mpc to within 1 deg^2 , providing ample opportunity for EM follow-ups and detect thousands of BNS mergers within its horizon redshift (see Sec. III for definitions of the horizon redshift and reach used in this paper) of $z = 0.9$. In contrast, the best 3G network would detect almost every BNS merger, some 50,000 of them, up to a redshift of $z = 0.9$, localizing **more than 20%** of them to better than 1 deg^2 , measuring distances to **more than a quarter of the mergers** to an accuracy better than **10%**. 3G observatories would have a reach of $z \lesssim 2.0$ to BNS mergers and a horizon redshift of $z \lesssim 10$.

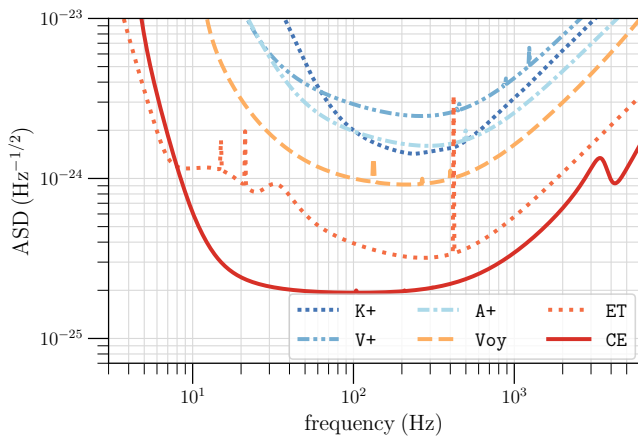


FIG. 1. Sensitivity of three generations of detectors: (i) Advanced-plus upgrade of LIGO (A+, Hanford, Livingston and India), Virgo (V+, Italy), and KAGRA (K+, Japan), (ii) Voyager upgrade of LIGO (Voy), and (iii) the next generation of detectors consisting of Cosmic Explorer (CE) and Einstein Telescope (ET). These sensitivities could be realized in the next 5, 10 and 15-20 years, respectively. See the text for different detector networks composed of one or more of these detectors considered in this paper. The noise curves are taken from the `kagra_plus`, `advirgo_plus`, `aplus`, `voyager_cb`, `et`, and `ce2_40km_cb` .txt-files inside `ce_curves.zip` file at <https://dcc.cosmicexplorer.org/CE-T2000007>.

Together with EM follow-up observations, such high-fidelity measurements would provide unprecedented access to fundamental questions in physics and astronomy including the nature of NSs, central engines of gamma-ray jets, production of heavy elements in the Universe, the expansion rate as a function of redshift and so on.

The Voyager network will have access to BBHs all the way to $z \sim 10$, detecting 50% of all mergers within a redshift of 2. It would achieve a signal-to-noise ratio of 100 for more than **50 mergers** each year. The best 3G network, on the other hand, will observe **almost all** BBH mergers within a redshift of 10, and **at least every other** source up to $z \approx 40$. **Tens** of BBH mergers will be observed each year with signal-to-noise ratios of 1000 or larger. Such exquisite observations will allow extremely accurate measurements of BH masses, their spins, distances, allowing us to address a variety of questions in astrophysics and dynamical spacetimes. These include, but not limited to, the astrophysical models of the formation and evolution of BBHs, tests of the BH no-hair theorem, exploration of the epoch of the formation of first stars at redshifts of 10-30, etc.

In this study we will focus in detail on the potential of the Voyager, ET, and CE detector generations using the Voy, ET, and CE noise curves shown in Fig. 1.

D. Organization of the paper

In Sec. II we will introduce the detector networks we are considering in this study, the properties of the source populations we are examining, and the Fisher-matrix package that was developed to assess the measurement capabilities of detector networks. In the rest of the paper we will introduce and discuss the metrics used to assess the relative performance of different networks. In Sec. III we will discuss the efficiency of detector networks in detecting signals as a function of redshift (or luminosity distance). Detection efficiency will inform us of the completeness of the observed population with respect to the full underlying population of mergers. Sec. III will also discuss the cosmic merger rate of compact binary coalescences inferred using current LIGO-Virgo observations, a model for the redshift evolution of the star formation rate and metallicity, and the resulting detections rates of the networks as functions of the redshift. In Sec. IV we will present the evaluation of the chosen detector networks and a forecast of the science questions that could be addressed by different generations of networks. Enabling multimessenger astronomy will require accurate 3D sky localization of compact binary coalescences, which will be the focus of Sec. V. This Section will also include forecasts for early warning alerts that would be possible with future detectors, with alerts sent to astronomers 10 minutes, 5 minutes and 2 minutes before the merger occurs and the corresponding 3D sky localization of the event. **Each year, the 3G network of CE and ET will observe hundreds of events with SNRs larger than 300 and once every other month, we can expect to detect events with stupendously large SNRs of 1000.** Sec. VI is devoted to discussing the science enabled by such rare events with SNRs larger than 300 or even 1000: such as observing higher multipole modes, testing the black hole no-hair theorem to exquisite precession, etc. Sec. VII provides

a brief summary, limitations of the study and how they might be improved and other studies that would be necessary to firm up the science potential of future detectors.

Unless specified otherwise, we use the geometric system of units in which Newton’s constant and the speed of light are both set to unity: $c = G = 1$.

II. NETWORKS, POPULATIONS, AND METHODOLOGY

A. Detector networks

In this paper we will consider six global networks composed of at least three detectors in some combination of the aforementioned detector generations as described below and summarized in Table I:

1. An A+ network consisting of the LIGO-Hanford (H), LIGO-Livingston (L), Virgo (V), KAGRA (K), and LIGO-India (I) detectors and denoted by HLVKI+ that could be operational in the next **5 years**,
2. A Voyager network consisting of three LIGO detectors (HLI) operating with Voyager technology in addition to A+ versions of Virgo and KAGRA and denoted by VK+HLIv that could be operating in the next **10 years**, and
3. Four 3G networks consisting of at least one 3G detector (Einstein Telescope (E) in Italy, Cosmic Explorer (C) in the US, and Cosmic Explorer South (S) in Australia) together with a combination of A+ sensitivity detectors, denoted as HLKI+E, VKI+C, KI+EC, and ECS. Such networks are expected to be operational in roughly **15–20 years**.

Although the choice of when a specific A+ configuration is included in a 3G network seems arbitrary, this resulted from our judgement that when a 3G detector comes online the corresponding region’s 2G+ detector(s) may no longer be in operation. For example, Virgo is not likely to be operational when ET is built, LIGO-Hanford and LIGO-Livingston are unlikely to operate at the same time as CE. Should it prove necessary to assess the performance of a network comprised of a different combination of detectors, e.g. HLI+C it would be straightforward to do so with GWBENCH.

Detectors	Network Name	Time-scale
LIGO (HLI+), Virgo+, KAGRA+	HLVKI+	2025-2030
LIGO (HLI-Voy), Virgo+, KAGRA+	VK+HLIv	2030-2035
ET, LIGO (HLI+), KAGRA+	HLKI+E	2035-2040
CE, Virgo+, KAGRA+ LIGO-I+	VKI+C	2040-2045
KAGRA+, LIGO-I+, ET, CE	KI+EC	2040-2045
ET, CE, CE-South	ECS	2040+

TABLE I. The network of GW detectors whose performance is evaluated using quantitative metrics discussed in Sec. III–VI. Note that the time-scale of operation of the various networks is our best guess estimate of when a given network is likely to operate, they do not correspond to any official projections.

B. Source populations

Throughout this paper, we examine two source populations containing either BNSs or BBHs. Each population was uniformly distributed in six redshift bins, $z \in [0.02, 0.5], [0.5, 1], [1, 2], [2, 4], [4, 10], [10, 50]$, with 250,000 injections per bin and converted to luminosity distance D_L using the PLANCK18 cosmology of ASTROPY. The injections were further uniformly sampled over sky positions (α and $\cos(\delta)$) and binary orientation angles ($\cos(\iota)$ and ψ), with right ascension α , declination δ , inclination ι , and polarization angle ψ . The injected spins were chosen to be aligned with the orbital angular momentum ($\chi_{1x} = \chi_{1y} = \chi_{2x} = \chi_{2y} = 0$) while the z -components were uniformly sampled, for BNS $\chi_{1z}, \chi_{2z} \in [-0.05, 0, 0.5]$ and for BBH $\chi_{1z}, \chi_{2z} \in [-0.75, 0, 0.75]$. The BNS masses were chosen to be normally distributed in $[1, 2] M_\odot$ with mean $\mu = 1.35 M_\odot$ and standard deviation $\sigma = 0.15 M_\odot$. The BBH masses were chosen to follow the POWER+PEAK distribution described in the Second Gravitational-Wave Transient Catalog population paper [73], but with the secondary mass sampled uniformly in $[5 M_\odot, m_1]$. These parameters are summarized in Tab. II.

C. Analysis methodology

We assess the performance of the chosen GW networks using a fast, Fisher-information [74–76] based Python package, GWBENCH, that we developed and made publicly available [77]. The Fisher information formalism approximates the parameter posteriors to be Gaussian (assuming Gaussian noise), provides an analytic recipe to calculate the covariance matrix of the posteriors, and thus allows the computation of measurement error estimates for the gravitational waveform parameters. The implementation in GWBENCH incorporates the effect of Earth’s rotation, which is important for long-lasting waveform, and numerical differentiation schemes, enabling access to the host

Population	BNS	BBH
m_1	Gaussian ($\mu = 1.35 M_\odot, \sigma = 0.15 M_\odot$)	POWER+PEAK [73]
m_2	Gaussian ($\mu = 1.35 M_\odot, \sigma = 0.15 M_\odot$)	uniform in $[5 M_\odot, m_1]$
χ_{1x}, χ_{2x}	0	
χ_{1y}, χ_{2y}	0	
χ_{1z}, χ_{2z}	uniform in $[-0.05, 0.05]$	uniform in $[-0.75, 0.75]$
z	uniform in six bins: $[0.02, 0.5], [0.5, 1], [1, 2], [2, 4], [4, 10], [10, 50]$	
D_L	convert z via ASTROPY.PLANCK18	
$\cos(\iota)$	uniform in $[-1, 1]$	
α	uniform in $[0, 2\pi]$	
$\cos(\delta)$	uniform in $[-1, 1]$	
ψ	uniform in $[0, 2\pi]$	
ι_c, φ_c	0	

TABLE II. Sampling parameters for the BNS and BBH populations.

of gravitational waveform models in LAL, the LSC Algorithm Library [78]; ultimately enabling the use of more sophisticated waveform models and therefore more accurate estimates. gwBENCH packs this in an easy-to-use fashion and further gives access to signal-to-noise ratio (SNR) calculations, various detector locations and noise curves, and basic sampling methods.

Thus, the package allows us to make a comprehensive evaluation of the six chosen detector networks using well-defined performance metrics: SNR ρ , 90%-credible sky area Ω_{90} , and measurement errors estimates of gravitational waveform parameters. The latter depend on the waveform models employed: For the BNS population we use the IMRPhenomD_NRTidalv2 model [79] to accurately capture tidal effects. For the BBH population we use the IMRPhenomHM [80] model to accurately capture the dynamics of sub-dominant modes beyond the quadrupole that are important for highly mass-asymmetric systems which our BBH population includes. We perform the Fisher analysis over 9 parameter for both populations: chirp mass \mathcal{M} , symmetric mass ratio η , luminosity distance D_L , time and phase of coalescence t_c , ϕ_c , and the aforementioned binary orientation angles ι , ψ and sky positions α , δ . The Fisher analysis is performed in frequency domain from $f_L = 5$ Hz to $f_U = N f_{\text{isco}}$ in $df = 1/16$ Hz steps. N is chosen to be 4 for IMRPhenomD_NRTidalv2 and 8 for IMRPhenomHM to include the full ringdown dynamics. In either case, we truncated f_U above 1024 Hz to improve performance since the detector noise curves make waveform contributions above these frequencies negligible. The frequency at the innermost, stable, circular orbit for a binary of total mass M is defined as $f_{\text{isco}} = (6^{3/2} \pi M)^{-1}$.

The reported performance metrics were chosen on the basis of metrics that were designed to accomplish specific science goals by the Cosmic Explorer Project. The raw data for a variety of other networks is available online as well as the associated scripts to produce the desired data products described in this paper, see Appendix C.

III. MERGER AND DETECTION RATES: COMPACT BINARIES THROUGHOUT THE COSMOS

A. Detector response including its motion relative to a source

a. Antenna pattern Gravitational-wave detectors are quadrupole antennas and their sensitivity to sources has the same anisotropic response as that of a quadrupole (see, e.g., Ref. [81]) with the additional complication that GWs are metric perturbations with two independent polarizations h_+ and h_\times . The response of a GW detector to signals coming from a direction (θ, ϕ) is

$$h^{(A)}(t, \boldsymbol{\mu}) = F_+^{(A)}(\alpha, \delta, \psi; R_A, \alpha_A, \beta_A, \gamma_A) h_+(t, \boldsymbol{\lambda}) + F_\times^{(A)}(\alpha, \delta, \psi; R_A, \alpha_A, \beta_A, \gamma_A) h_\times(t, \boldsymbol{\lambda}), \quad (1)$$

where $F_+^{(A)}$ and $F_\times^{(A)}$ are the quadrupole antenna pattern functions of a detector indexed by A in the long-wavelength approximation (which is sufficiently accurate even in the case of 3G detectors that will be tens of kilometers long, except for small corrections that might be needed at kilohertz frequencies), (α, δ) are the source's right ascension and decli-

nation in the geocentric coordinate system, ψ is the polarization angle, $(R_A, \alpha_A, \beta_A, \gamma_A)$ are the altitude, latitude, longitude, and the angle from local north to the x -arm of detector A , $\boldsymbol{\lambda} = \{\lambda_k\}$, $k = 1, \dots, n_\lambda$, is the parameter vector describing the strain at the location of the detector and $\boldsymbol{\mu} = \{\mu_K\} = \{\theta, \varphi, \psi, \boldsymbol{\lambda}\}$, $K = 1, \dots, n_\mu$, is the full parameter vector including the source's position in the sky and the polarization angle.

b. Strain parameters For a compact binary system on a quasi-circular inspiralling orbit, $\boldsymbol{\lambda}$ consists of the luminosity distance D_L to the source, the orientation of the orbit relative to the line-of-sight ι , the redshifted masses (m_1, m_2) and spins (S_1, S_2) of the companions, the epoch of coalescence t_c taken to be the time when the amplitude of the response, which grows until the compact binary coalesces and then decays down rapidly, reaches its maximum value, and φ_c the phase of the signal at that epoch.

It is often convenient to use dimensionless spins (χ_1, χ_2) , which, in geometric units, are given by $(\chi_1, \chi_2) = (S_1/m_1^2, S_2/m_2^2)$. The magnitudes of the dimensionless spin vectors lies between $[0, 1]$. Likewise, in the post-Newtonian expansion of the waveform phase the chirpmass $\mathcal{M} = (m_1 m_2)^{3/5} / (m_1 + m_2)^{1/5}$ and symmetric mass ratio $\eta = m_1 m_2 / (m_1 + m_2)^2$ appear more naturally than the component masses [82].

c. Time-dependent antenna pattern Note that the position of the source in the sky is given in the geocentric coordinate system with respect to which the detector's position, described by angles $(\alpha_A(t), \beta_A(t))$, varies due to Earth's rotation. The relative motion of a detector with respect to a source induces amplitude modulation in the observed signal due to the changing antenna pattern functions in the direction of a source. The value of the antenna pattern changes at most by a magnitude of order $\Delta h \sim |\sin(2\Delta\alpha)|$, where $\Delta\alpha$ is the change in the right ascension to the source relative to the detector; $\Delta h \sim 1$ over a six hour period. Since we can determine the amplitude of a signal to an accuracy of order $1/\rho$, where ρ is the SNR, the amplitude modulation could be important for signals that last for more than ~ 30 minutes at an SNR of $\rho = 10$, and for even shorter periods for louder events.

d. Detector location-dependent phase factor In addition, a detector location-dependent phase factor should be considered to account for the changing arrival times of the signal at the detectors relative to the geocentric coordinate system. This is accomplished by multiplying the Fourier transform of the response function $\tilde{h}(f)$ by the appropriate phase factor:

$$\tilde{h}(f) \rightarrow \tilde{h}(f) \exp \left[i 2\pi f \frac{\mathbf{r}(t) \cdot \mathbf{n}(\alpha, \delta)}{c} \right],$$

where $\mathbf{r}(t)$ is the position vector of the detector on Earth, \mathbf{n} is a unit vector in the direction of the source, and c is the speed of light. For signals that last for periods greater than 30 minutes, this additional phase factor in the response could further improve the localization of the source and is most relevant for BNS sources in ET.

e. Frequency modulation The frequency modulation due to Earth's rotation, however, is not important as the fractional change in frequency is expected to be negligible over the observation period of a signal: $\Delta f/f = v_{\text{rot}} \ll 1/P_{\text{max}}$, where $v_{\text{rot}} = 1.5 \times 10^{-6}$ is Earth's rotational velocity at the equator,

and P_{\max} is the maximum duration for which a signal lasts in the detector's sensitivity bandwidth. P_{\max} is the largest for BNS signals and varies from a few minutes to several hours depending on the lower-frequency cutoff of a detector below which contribution to the SNR of a signal is negligible. Thus, the change in frequency is not discernible for compact binary coalescence sources and frequency modulation can be neglected.

B. Network efficiency

Having defined the response of a detector to a GW signal we next turn to defining the efficiency of a network of detectors, which would be required in computing the detection rate of a network. The *efficiency* $\epsilon(z)$ of a detector or a network of detectors at a given redshift or luminosity distance is defined as the fraction of all sources within that redshift for which the matched filter SNR ρ of the network is larger than a preset threshold ρ_* . To this end, the matched filter SNR ρ of a network of n_D detectors to an incident signal is defined as:

$$\rho^2 = \sum_{A=1}^{n_D} \rho_A^2, \quad \rho_A^2 = 4 \int_{f_L}^{f_U} \frac{|\tilde{h}^{(A)}(f)|^2}{S_h(f)} df, \quad (2)$$

where $h^{(A)}$ is the detector response of detectors $A = 1, \dots, n_D$, given in Eq.(1), f_L and f_U are the detector- and signal-dependent lower and upper frequency cutoffs chosen so that there is negligible SNR outside that interval. The SNR depends on both the intrinsic and extrinsic parameters of the source: the source's masses and spins, distance, sky position, and orientation.

In order to compute the efficiency of a network at a given redshift z we inject signals in the interval z and $z + dz$ with their intrinsic and extrinsic parameters (masses and spins of the binary, the four angles giving the position of the binary and its orientation) distributed as in Tab. II and count the number of sources for which the SNR was larger than ρ_* :

$$\epsilon(z, \rho_*) = \frac{1}{N_z} \sum_{k=1}^{N_z} \Pi(\rho_k - \rho_*), \quad \Pi(x) = \begin{cases} 0, & \text{if } x \leq 0 \\ 1, & \text{if } x > 0. \end{cases} \quad (3)$$

where N_z is the number of sources in the simulation in the redshift interval $[z, z + dz]$, ρ_k is the SNR of the k^{th} event in the injection list, and $\Pi(x)$ is the Heaviside step function. We repeat this process from $z = 0.01$ to $z = 50$, thereby obtaining the efficiency curves shown in Fig. 2, top two panels, for different detector networks considered in this study. The well-known *sigmoid* functions with three parameters are a good fit to the efficiency curves

$$f_{\text{sigmoid}} = \left(\frac{1+b}{1+b e^{ax}} \right)^c. \quad (4)$$

Appendix C lists the best-fit parameters a , b , and c for the various networks. Note that for a given source population the network efficiency depends only on the SNR threshold ρ_* and not how sources are distributed as a function of redshift. The detection rate of networks for different a source distribution

than the one considered in this study can be computed using the efficiency curves provided here.

The network efficiency is plotted for two choices of the SNR threshold, $\rho_* = 10$ and $\rho_* = 100$. The lower value corresponds to the smallest SNR at which a confident detection can be made by a detector network while the larger value is included to show redshift/distance from within which one can observe signals with high-fidelity. In Fig. 2, there are a pair of fitting lines with the same color for a given network but distinguished by circles for $\rho_* = 10$ and squares for $\rho_* = 100$, the one with greater efficiency corresponds to the lower ρ_* .

The network efficiency can be used to characterize the *completeness* of the survey of a detector network. For example, while the VK+HLIV network is **60%** complete for BNS sources up to a redshift of $z \simeq 0.2$, the ECS network achieves **60%** completeness up to a redshift of $z \simeq 2$, as can be seen from the top panels of Fig. 2. Most remarkably, the ECS network will be 90% complete to BNS mergers within $z = 1$ —the redshift limit up to which most current and future EM telescopes will have the ability to carry out follow-up observations of the mergers. Access to such a complete sample would help in understanding the physics and astrophysics of BNS mergers with little observational bias.

C. The reach and horizon redshift of a network

In the following, we refer to the *reach* z_r of a network as the redshift at which the detection efficiency is $\epsilon = 0.5$, which means the network is capable of detecting at least half of the source population at any redshift up to its reach. On the contrary, the *horizon redshift* of a network is the maximum redshift at which the network can detect sources at the SNR threshold, taken to be $\rho_* = 10$ in this study. For a single interferometer an optimally oriented binary, i.e. the orbital and detector planes are parallel, would be detected at threshold SNR at horizon distance. For a network, however, the horizon redshift is calculated numerically and we approximate it as the distance at which the network efficiency falls to $\epsilon = 0.001$. We assume that a signal with an SNR of $\rho \geq 10$ would be detected with good confidence. The reach and horizon of a network can also be assessed for other SNR threshold values. In Tab. III we provide the reach and horizon of all the networks for BNS and BBH mergers for two threshold SNR values: detections with $\rho \geq 10$ and exceptionally loud signals with $\rho \geq 100$. Note that the GW literature has many different measures of reach and horizons and not all agree with the ones defined here.

D. Merger and detection rates

The merger rate of compact binaries in the local Universe comes from the first and second Gravitational-Wave Transient Catalogs GWTC-1 and GWTC-2 [6, 7]. They contain 2 BNS and 44 stellar-mass BBH mergers as enumerated in Table 1 of Ref. [73]. The inferred local merger rates (i.e. at redshift $z = 0$) were found to be $R_{\text{BNS}} = 320 \text{ Gpc}^{-3} \text{ yr}^{-1}$ for BNS mergers and $R_{\text{BBH}} = 24 \text{ Gpc}^{-3} \text{ yr}^{-1}$ for BBH mergers [16].

LIGO and Virgo do not observe coalescences at cosmological distances (i.e. $z \gtrsim 0.5$) but future detectors will. Several

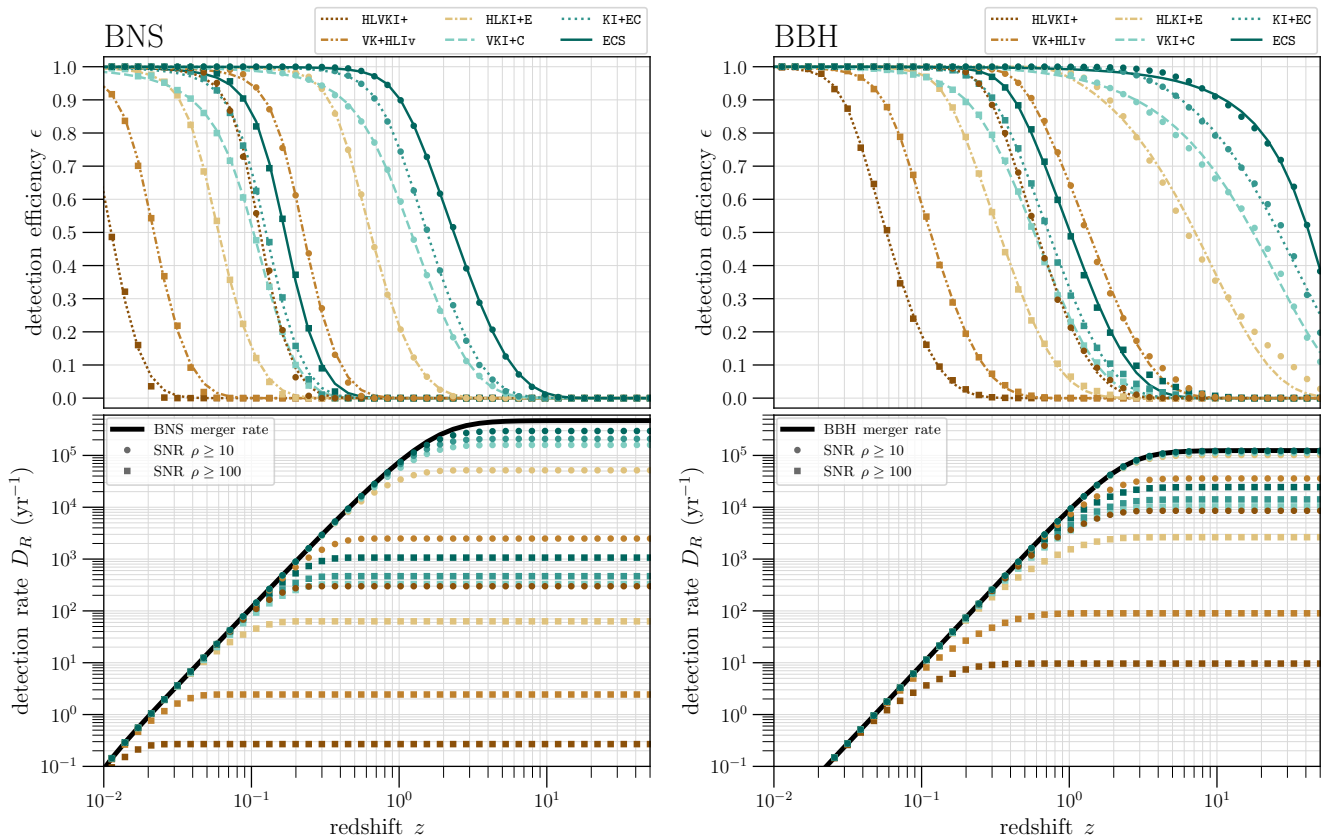


FIG. 2. Detection efficiencies ϵ and detection rates D_R of the six studied A+, Voyager and 3G networks are plotted as functions of redshift z . The circles (squares) denote the values for events with $\text{SNR } \rho \geq 10$ ($\rho \geq 100$). The thick, black lines in the rate panels are the cosmic BNS and BBH merger rates, see Sec. III. The fit lines in the efficiency panels are sigmoid fits with $f_{\text{sigmoid}} = \left(\frac{1+b}{1+b e^{ax}} \right)^c$.

TABLE III. The reach z_r and horizon z_h of the considered networks for BNS and BBH signals with $\text{SNRs } \rho \geq 10$ or $\rho \geq 100$. Here we define the reach (horizon) as the redshift at which a given network detects 50% (0.1%) of the injections with the specified SNR or louder. Please refer to the detection efficiency panels of Fig. 2 for a visual representation.

SNR ρ	BNS				BBH			
	≥ 10		≥ 100		≥ 10		≥ 100	
	z_r	z_h	z_r	z_h	z_r	z_h	z_r	z_h
HLVKI+	0.11	0.42	0.011	0.040	0.60	3.7	0.058	0.33
VK+HLIV	0.22	0.90	0.022	0.087	1.4	9.7	0.11	0.68
HLKI+E	0.64	3.3	0.060	0.27	7.1	> 50	0.33	2.2
VKI+C	1.2	8.1	0.10	0.46	18	> 50	0.58	4.3
KI+EC	1.5	9.5	0.13	0.51	26	> 50	0.72	4.9
ECS	2.3	15	0.17	0.67	42	> 50	1.0	7.1

factors affect the rate as a function of redshift. Following Ref. [83] we take into account three principal ones: (1) The rate at which stars form, (2) the delay between the formation of a compact binary and its merger and, for BBH systems, and (3) the variation of metallicity with redshift.

The star formation rate (SFR) initially increases as a function of redshift, peaking around $z \sim 1-2$ after which it rapidly falls

off. We will take the compact binary formation rate, and hence the merger rate, to essentially follow the SFR except that there will be a delay t_f between when a compact binary forms and the epoch when it merges. Finally, the metallicity plays a crucial role in the formation of BHs due to its effect on stellar winds, which must be folded into the calculation of rates. In addition, we must be mindful of the fact that the cosmological volume element (dV/dz) corresponding to a redshift interval dz is itself a function of redshift due to the Hubble expansion and the Universe was smaller at earlier times.

Compact binaries that form at redshift z' merge at redshift z after a delay time t_d . The delay time is not fixed but given by a probability density $P(t_d)$. Thus, if $R_f(z')$ denotes the rate density of the *formation* of compact binaries (which is assumed to be proportional to the SFR) then the rate density of *mergers* in the source's frame $R_{\text{src}}(z)$ is obtained by integrating over all possible time delays,

$$R_{\text{src}}(z) = A \int_{t_d^{\min}}^{t_d^{\max}} R_f(t(z) - t_d) P(t_d) dt_d, \quad (5)$$

where t_d^{\min} and t_d^{\max} denote the smallest and largest possible time delays and the normalization constant A is chosen so that local rate $R_{\text{src}}(0)$ is consistent with the rate inferred using the GWTC-2 catalog [73]: $R_{\text{src}}^{\text{BNS}}(0) = 320_{-240}^{+490} \text{Gpc}^{-3} \text{yr}^{-1}$ and $R_{\text{src}}^{\text{BBH}}(0) = 23_{-7}^{+14} \text{Gpc}^{-3} \text{yr}^{-1}$.

The delay-time distribution is not very well known but could be inferred accurately from future observations. As is customary, we take $P(t_d)$ to be Jeffery's prior $P(t_d) \propto 1/t_d$. With the normalization it becomes:

$$P(t_d) = \frac{\ln(t_d^{\max}/t_d^{\min})}{t_d}. \quad (6)$$

For this prior, most of the contribution to the density comes from near t_d^{\min} which we set to be $t_d^{\min} = 100$ Myr for BNS and $t_d^{\min} = 10$ Myr for BBH mergers. We take $t_d^{\max} = 10$ Gyr in both cases.

Since $R_{\text{src}}(z)$ is the merger rate *density* the merger rate is

$$\mathcal{R}_{\text{src}}(z) = R_{\text{src}}(z) \frac{dV}{dz} \quad (7)$$

where $dV(z)/dz$ is the comoving volume element. An observer in the local Universe would measure the rate of mergers to be a factor $(1+z)$ smaller than in the source's frame, i.e. $\mathcal{R}_{\text{obs}}(z) = \mathcal{R}_{\text{src}}(z)/(1+z)$. A network of detectors, however, would not observe all the mergers that would occur at a given redshift but only a fraction $\epsilon(z, \rho_*)$ determined by the network's efficiency, which in turn depends on the SNR threshold ρ_* . Thus, the detection rate, i.e. the number of detections per year, $D_R(z, \rho_*)$ observed up to redshift z is given by:

$$D_R(z, \rho_*) = \int_0^z \epsilon(z', \rho_*) \frac{R_{\text{src}}(z')}{1+z'} \frac{dV(z')}{dz'} dz'. \quad (8)$$

The BBH merger rate was chosen to follow the 'Madau-Dickinson-Belczynski-Ng' rate for field BHs described in [84]. For the BNS population we take the SFR to be that of Madau-Dickinson but neglect the effect of metallicity evolution as this is not as important for the formation of NSs.

The bottom panels of Figure 2 plot the detection rate D_R as a function of redshift for two choices of the threshold: $\rho_* = 10$ and $\rho_* = 100$. We will discuss the SNR distribution in the next Section.

IV. VISIBILITY AND MEASUREMENT QUALITY OF COMPACT BINARY MERGERS IN FUTURE DETECTORS

In the following we summarize the overall capabilities of the six studied networks for the BNS and BBH populations throughout the chosen redshift range $z \in [0.02, 50]$. As such we will make 'full-population' statements for the expected detection rates that each network should achieve given a set of targets for the performance metrics specified below.

Figs. 3 and 4 present the cumulative density functions (CDFs) for six performance metrics, SNR ρ , sky area Ω_{90} , fractional errors on chirpmass $\Delta M/M$ and luminosity distance $\Delta D_L/D_L$, and absolute errors on symmetric mass ratio $\Delta \eta$ and inclination angle Δi . Fig. 3 summarizes the BNS injections, while Fig. 4 shows the results for the BBHs. In both cases, the CDFs present the *relevant* data from the 1.5 million injections that were simulated in the redshift range and are shown to the 0.01%-level. Here, *relevant* data refers to (i) the entire injection set in case of the SNR sub panel, with $(\rho < 1)$ -events truncated, and (ii) the 'detectable' events with $\rho \geq 10$ for the remaining metrics. We show the respective histograms in Appendix A.

A. Incorporation of redshift-dependent merger rates

While the uniform sampling per redshift bin provides us with good parameter sampling, it also means that we need to scale the PDFs to capture the redshift-dependent merger rates as discussed in the previous section. For this purpose we divide the redshift range in $N = 150$ sub-bins, containing each $n_i \approx 10,000$ injections. Each sub-bin has an associated merger rate R_i , $i = 1, \dots, N$ computed following Sec. III, allowing us to define sub-bin probabilities as $p_i = R_i/R$ with $R = \sum_{i=1}^N R_i$. We then sample the N sub-bin indices i with probabilities p_i up to the desired number of BNS and BBH mergers, e.g. **10 years of mergers**, thus providing us with a number of samples n_i for each index i . Finally, we uniformly sample n_i injections from the simulated BNS and BBH mergers in the i -th sub-bin, thus resulting in a random sample of injections in each sub-bin with the desired total number of mergers in the total redshift range.

In order to mitigate sampling effects in the distribution tails we perform all analyses using a 10-year random sample of BNS and BBH mergers drawn from the simulated populations at the corresponding cosmic merger rates for the redshift range of interest. We show these 10-year samples in all histograms and scatter plots throughout this paper to better represent what each network is statistically capable to achieve and we mention this again in the captions of the respective figures. Similarly, all presented CDFs are calculated from these larger samples to improve the statistics. **In contrast**, we cite yearly detections rates for the studied networks both in the text and tables, in order to represent rates for a time-scale more akin to the observing runs of the LIGO and Virgo detectors. The rates are calculated from the respective CDFs and cosmic merger rates (visibility) or detection rates (measurement quality).

B. Signal visibility

The cosmic merger rate of BNS is of the order of 4.7×10^5 per year, but depending on the network we can only expect completenesses as low as $\sim 0.04\%$ in HLVKI+ and $\sim 0.4\%$ in VK+HLIv up to $\sim 51\%$ with three 3G detectors (ECS), see the SNR panel of Fig. 3. These percentages translate to approximately $\mathcal{O}(10^2)$, $\mathcal{O}(10^3)$, and up to $\mathcal{O}(10^5)$ BNS detections per year, respectively, summarized in Tab. IV. These raw numbers illustrate the stark difference in volume and corresponding merger rates that each network's reach encompasses: $z \sim 0.11$ for HLVKI+, $z \sim 0.22$ for VK+HLIv, and $z \sim 2.3$ for ECS (see Fig. 2). Further, Tab. IV indicates that we can expect a host of BNS events in the 'GW170817-class' with SNRs $\rho \geq 30$, while SNR values above 100 are only regularly observable in 3G networks. In fact, 3G networks containing a CE detector will observe such loud events at rates of the order 1/10 to 1/3 of all detections in a Voyager network.

The picture for BBH mergers, see the SNR panel of Fig. 4 and Tab. IV, is less skewed in favor of the 3G networks in comparison to the Voyager network since its redshift reach $z_r \sim 1.4$ extends into the peak of the Madau-Dickinson-Belczynski-Ng merger rate density; see [84]: Both HLVKI+ and VK+HLIv will detect $\mathcal{O}(10^3)$ and $\mathcal{O}(10^4)$ BBH mergers per year with completenesses of **5%** and **20%**, while the 3G networks will

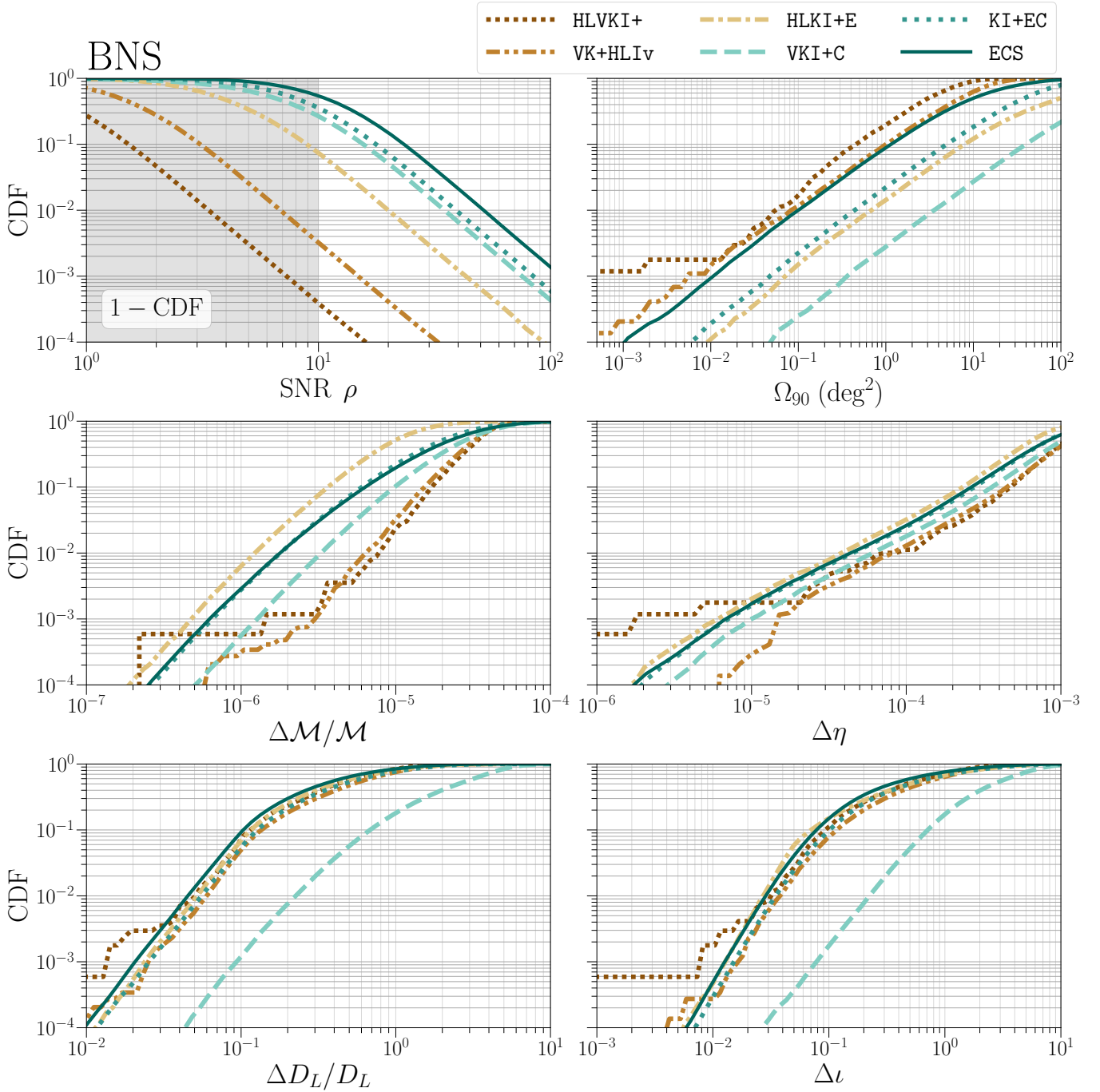


FIG. 3. Cumulative density function (CDF) for the SNR ρ , 90%-credible sky area Ω_{90} , fractional errors on chirpmass $\Delta M/M$ and luminosity distance $\Delta D_L/D_L$, and absolute errors on symmetric mass ratio $\Delta\eta$ and cosine of the inclination angle $\Delta \cos(i)$ for BNS mergers observed in the six studied A+, Voyager and 3G networks. The non-SNR panels are obtained for events with SNR $\rho \geq 10$, indicated by the non-shaded region in the SNR panel. The SNR CDF is flipped to highlight the behavior for large values.

observe $\mathcal{O}(10^5)$ BBH mergers with completenesses between 77% (HLKI+E) and 99% (ECS). In fact, all considered networks will detect BBH coalescences with SNRs above 100 albeit at horizon redshifts of $z_h \sim 0.33$, $z_h \sim 0.68$, and up to $z_h \sim 7.1$ and corresponding redshift reaches of $z_r \sim 0.06$, $z_r \sim 0.11$, and $z_r \sim 1.0$ for HLVKI+, VK+HLIV, and ECS, respectively. Hence, the difference between these networks comes down to the 3G networks' reach for BBHs extending beyond redshift 10

and the resulting completeness of the observable population at high redshifts: KI+EC and ECS will detect essentially all BBHs signals at the cosmic merger rate of $\sim 1.2 \times 10^5 \text{ yr}^{-1}$.

While the yearly rates for all six networks far exceed the number of events observed with the current generation of detectors [6, 7], the differences between these future networks are still crucial in their impact for astrophysics, cosmology, tests of general relativity, and dense matter physics. Fig. 5 captures

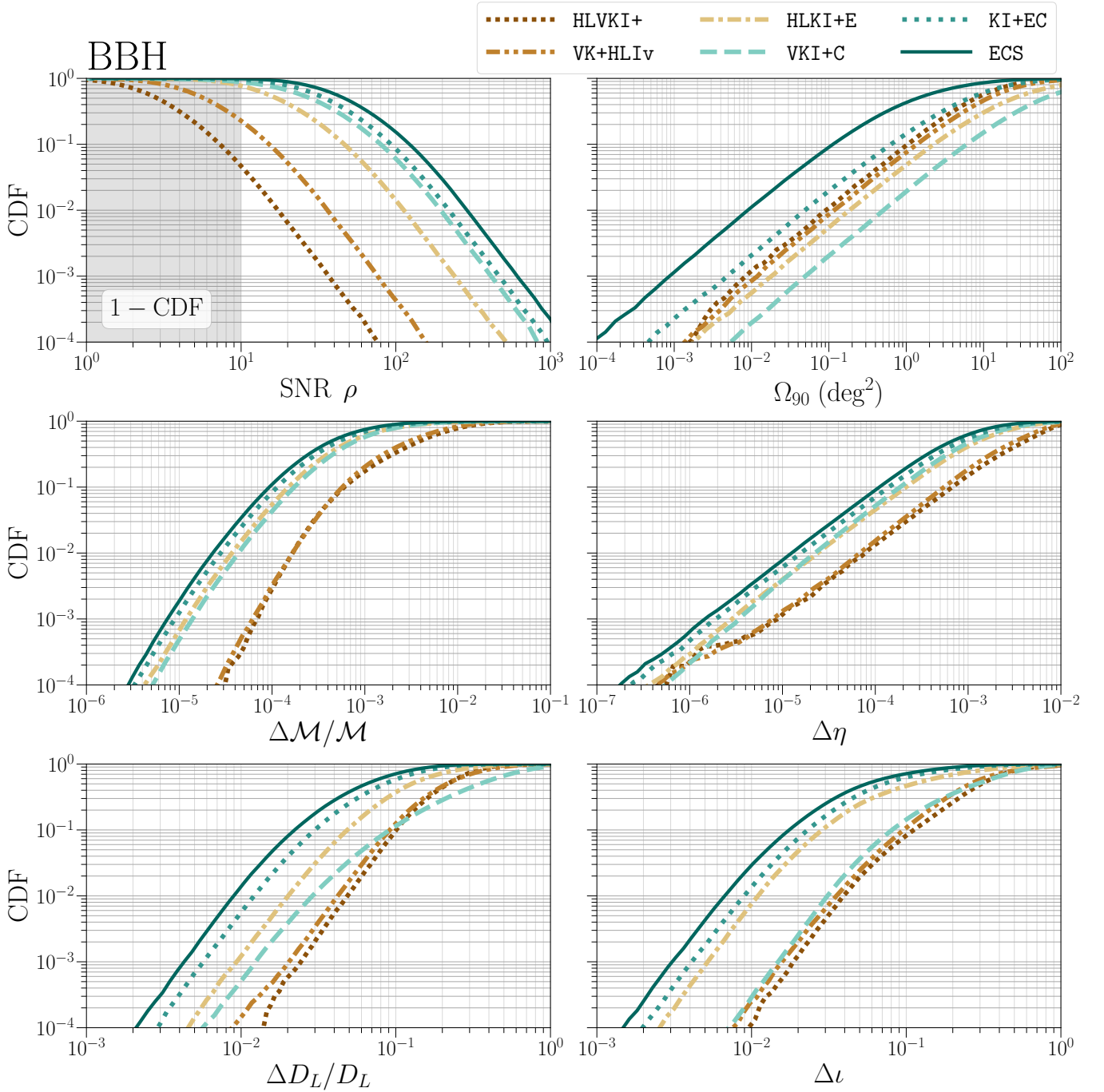


FIG. 4. Cumulative density function (CDF) for the SNR ρ , 90%-credible sky area Ω_{90} , fractional errors on chirpmass $\Delta\mathcal{M}/\mathcal{M}$ and luminosity distance $\Delta D_L/D_L$, and absolute errors on symmetric mass ratio $\Delta\eta$ and cosine of the inclination angle $\Delta\cos(i)$ for BBH mergers observed in the six studied A+, Voyager and 3G networks. The non-SNR panels are obtained for events with SNR $\rho \geq 10$, indicated by the non-shaded region in the SNR panel. The SNR CDF is flipped to highlight the behavior for large values.

these differences and visually presents what signal loudness and sky localization distributions to expect from GW events throughout the redshift range for the studied networks.

Only 3G networks will deliver an abundance of exceptionally loud BNS signals with SNRs above 100; even to cosmological distances of $z \lesssim 0.5$. Such events will allow us to probe the nuclear regime with high fidelity, constrain the dense matter of equation of state, and explore the BNS post-inspiral regime.

For both the BNS and BBH coalescences the differences in reach and horizon distances, see Tab. III, means that not only a larger, but also older part of the BNS and BBH populations can be studied with 3G networks. These networks will observe almost all BNS and BBH mergers up to luminosity distances of $\lesssim 2$ Gpc and $\lesssim 25$ Gpc, respectively. Their horizons lie at $z_h \gtrsim 10$ for BNSs and beyond ~ 50 for BBHs, in contrast to the Voyager network with $z_h \sim 0.9$ and $z_h \sim 9.7$, respectively.

TABLE IV. Cosmic merger rates (per year) of BNS and BBH mergers in the Universe and the number that would be observed by different detector networks each year with $\rho \geq 10$, $\rho \geq 30$, and $\rho \geq 100$, where ρ is the signal-to-noise ratio. Due to uncertainty in the various quantities that go into the calculation these numbers are no more accurate than one or two significant figures. Fig. 2 sketches the merger rate and detection rate as a function of redshift.

Cosmic rate	BNS			BBH		
	4.7×10^5			1.2×10^5		
SNR ρ	≥ 10	≥ 30	≥ 100	≥ 10	≥ 30	≥ 100
HLVKI+	170	6	0	6,500	210	5
VK+HLIv	1,800	58	2	26,000	1,900	60
HLKI+E	40,000	1,500	34	95,000	27,000	2,000
VKI+C	130,000	8,900	170	110,000	60,000	8,500
KI+EC	150,000	8,900	330	120,000	74,000	9,400
ECS	240,000	21,000	560	120,000	91,000	18,000

This means that a 3G network could observe BNS coalescences from roughly 500 Myr and BBH mergers from less than 50 Myr after the Big Bang, thus expanding their observational potential deep into the realm of the early Universe! While the expectations for mergers in this regime are very low, population III stars and primordial BHs could pose potential progenitor and source systems, to which non-3G networks would be blind.

Lastly, the sheer abundance of loud events up to far redshifts will further enable astronomers and cosmologists to better understand source population demographics as well as trace and correlate the large-scale structure of the Universe with these mergers. Further, louder and more abundant signals will be a treasure trove for tests of general relativity which benefit from the outright signal strengths but also the potential of signal binning.

We will examine rare, extremely loud signals with SNRs $\rho \gtrsim 300$ in Sec. VI.

C. Measurement quality

The three-dimensional localization of a source, on the sky and in luminosity distance, is crucial in enabling a multitude of science, especially for BNS mergers which can exhibit observable electromagnetic (EM) counterparts. Hence, we summarize the expected detection rates of events with 90%-credible sky area $\Omega_{90}/\text{deg}^2 \leq 0.01, 0.1, 1$ and fractional luminosity distance errors $\Delta D_L/D_L \leq 0.01, 0.1$ in Tab. V. The visual representations in form of CDFs can be found in the Ω_{90} - and $\Delta D_L/D_L$ -panels of Fig. 3. We will further expand our examination of the potential to enable multi-messenger astronomy at redshifts $z \leq 0.5$ in Sec. V.

GW190814 [16] is the best-localized, observed GW event so far, with a 90%-credible sky area of 19 deg^2 and a luminosity error of about 19%. In comparison, both HLVKI+ and VK+HLIv will detect $\mathcal{O}(10)$ to $\mathcal{O}(10^2)$ BNS sources per year with sky areas below 1 deg^2 and 10% luminosity distance errors, with BBH-numbers being an order of magnitude larger. Both networks will further be capable to observe $\mathcal{O}(10)$ BNS and $\mathcal{O}(10^2)$ BBH mergers per year with sky areas below 0.1 deg^2 and a

TABLE V. Detection rates of BNS and BBH mergers from the full redshift range $z \in [0.02, 50]$ to be observed by different detector networks each year with $\Omega_{90}/\text{deg}^2 \leq 1, 0.1, 0.01$ as well as $\Delta D_L/D_L \leq 0.1, 0.1$, where Ω_{90} is the 90%-credible sky area and D_L the luminosity distance. These detection rates are calculated for events with SNR $\rho \geq 10$. Due to uncertainty in the various quantities that go into the calculation these numbers are no more accurate than one or two significant figures.

Metric	$\Omega_{90} (\text{deg}^2)$			$\Delta D_L/D_L$	
	≤ 1	≤ 0.1	≤ 0.01	≤ 0.1	≤ 0.01
<i>BNS</i>					
HLVKI+	34	3	0	14	0
VK+HLIv	180	22	3	100	0
HLKI+E	600	59	4	2,700	2
VKI+C	250	32	2	140	1
KI+EC	3,500	380	25	7,500	8
ECS	20,000	2,600	210	23,000	29
<i>BBH</i>					
HLVKI+	660	70	8	610	0
VK+HLIv	1,800	240	20	3,500	4
HLKI+E	4,100	580	53	37,000	130
VKI+C	2,400	200	20	12,000	64
KI+EC	18,000	2,300	220	69,000	660
ECS	50,000	12,000	1,500	84,000	1,900

hand full of BBH signals localized to less than 0.01 deg^2 .

The picture for the 3G networks is more differentiated than it was for the signal visibility. These networks differ in the number of 3G detectors per network with one in HLKI+E and VKI+C, two in KI+EC, and three in ECS. Since especially sky area, but also luminosity distance measurements improve dramatically with more detectors in a network, the number of more sensitive 3G detectors has a strong effect on the measurement quality. This is illustrated by the increase of green-colored points in the KI+EC and ECS panels of Fig. 5, indicating their improved sky localization capabilities.

Consequently, these networks will detect BNS coalescences localized to within a 90%-credible sky area smaller than $(1, 0.1, 0.01) \text{ deg}^2$ on the order of $(\mathcal{O}(10^2), \mathcal{O}(10), \mathcal{O}(1))$ per year in HLKI+E and VKI+C, $(\mathcal{O}(10^3), \mathcal{O}(10^2), \mathcal{O}(10))$ per year in KI+EC, and $(\mathcal{O}(10^4), \mathcal{O}(10^3), \mathcal{O}(10^2))$ per year in ECS. Further, fractional luminosity distance errors smaller than $(0.1, 0.01)$ will be observed at rates of the order $(\mathcal{O}(10^2), \mathcal{O}(1))$ per year in VKI+C, $(\mathcal{O}(10^3), \mathcal{O}(1))$ per year in HLKI+E and KI+EC, and $(\mathcal{O}(10^4), \mathcal{O}(10))$ per year in ECS. The rates for BBHs are 2-10 times larger per year, with the notable exception that HLKI+E, VKI+C, KI+EC, and ECS will observe $(\mathcal{O}(10)$ to $\mathcal{O}(10^3))$ BBH mergers per year down to sub-1% accuracies in luminosity distance; roughly 60 times the BNS numbers.

The sky localization capabilities of all networks, but VKI+C, scale with the networks' sensitivities (Tab. IV). In contrast, while VKI+C observes four times as many events as the Voyager network VK+HLIv and even 100x the number of $\rho \geq 100$ -events, both networks perform equally in terms sky localization. This is a clear indication to the importance of both the number of detectors within in a network and their sensitivity. With

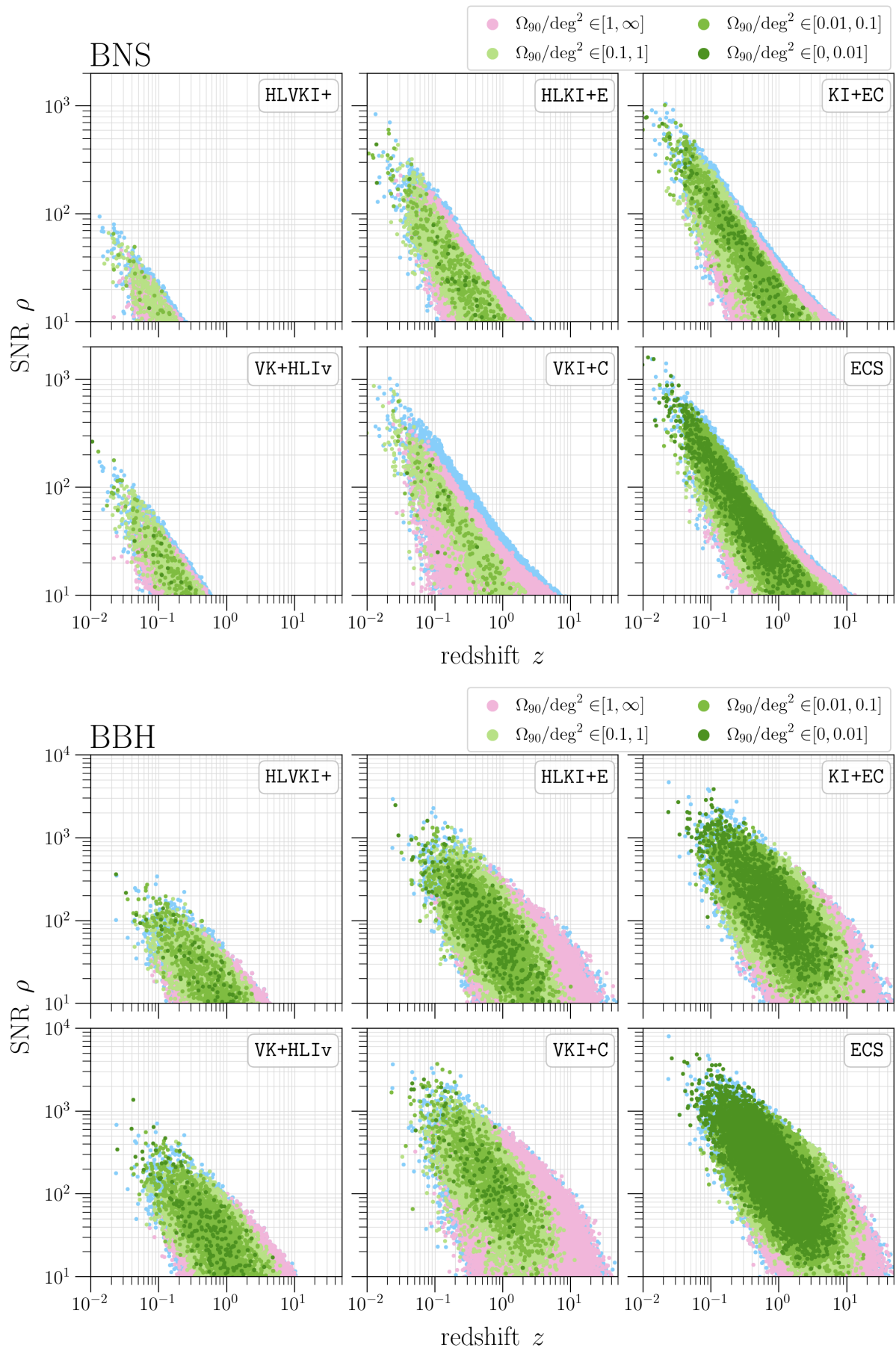


FIG. 5. The scatter plots illustrate the correlations between redshift z , SNR ρ , and 90%-credible sky area Ω_{90} for BNS (top) and BBH (bottom) mergers in the six studied A+, Voyager and 3G networks. The blue dots indicate injections without Ω_{90} -information due to ill-conditioned Fisher matrices. The plots were generated from injections corresponding to an observation time of **10 years**.

only four detector sites and only one detector beyond the A+ generation, VKI+C’s sky localization capabilities are inferior to a network of five detectors, three of which operating at Voyager sensitivities. Ultimately, it performs equally due to its farther reach and thus larger base detection rate. In Appendix B we examine the differences between networks with four different CE configurations: i) the current single 40 km arm length, ii) a single 20 km arm length, iii) two CEs with 20 km arm lengths, and iv) two CEs with 20 and 40 km arm lengths.

As was mentioned above, the three-dimensional localization of a GW source is extremely important for BNS coalescences which exhibit EM counterparts, such as the gamma-ray burst GRB 170817A and kilonova AT2017gfo associated with the GW event GW170817 [10]. Unfortunately, such coincident detections with bright, EM transients like GRBs require the emission of the burst in our direction while being in the field-of-view (FOV) of operating telescopes. Thus, if this initial pointer is missed or poorly localized itself, the EM follow-up will be hampered. As such the second BNS event GW190425, observed by the LIGO and Virgo detectors, did not appear to have a coincident gamma-ray burst, its location was not determined, and the potential counterpart was not studied in the EM spectrum.

If the GW signal itself already were to point to the source, by pin-pointing the sky location to within a 90%-credible sky area that telescopes can quickly survey, a strong, coincident EM would not be required to find the fainter counterpart. Further, the identification of the signal’s host galaxy allows the astronomy community to improve their surveys of the Universe’s large-scale structure both locally but also in the distant Universe with BBHs. Besides, measurements of the host’s redshift in conjunction with an accurate estimate of the luminosity distance from the GW signal could enable high-fidelity measurements of the Hubble constant in the local Universe to the level needed to resolve the Hubble-Lemaître tension with a single compact binary coalescence [54]. We examine the potential of the chosen networks in enabling multi-messenger astronomy in the next section.

V. ENABLING MULTI-MESSENGER ASTRONOMY

The EM follow-up campaign of the BNS event GW170817 resulted in the identification of the counterpart and observation of the afterglow in the entire EM spectrum, providing a treasure trove of data that has impacted several areas in fundamental physics, astrophysics and cosmology. As such the synergy of GW and EM observations of compact binary coalescences in the readily EM-observable Universe, $z \leq 0.5$, will be of paramount importance in the coming decades. In this section we examine how well each network will localize BNS mergers in the GW window enabling the potential for EM follow-up irrespective of a loud EM transient such as a gamma-ray burst. Further, we illustrate each network’s capabilities for early warning, i.e. both the detection and sky localization of a compact binary during the inspiral ahead of the merger.

Tab. VI presents the FOVs for 13 current or planned EM telescopes that have the capability to slew and follow-up GW detections. When considering these FOVs it is important to remember that they represent the sky area the respective tele-

scope can observe without any tiling: It is not uncommon for EM telescope to observe larger FOVs during a follow-up campaign by tiling the search region with up to ~ 10 segments.

EM telescope	FOV (deg ²)
Rubin Observatory	9.6
EUCLID	0.54
WFIRST	0.28
Chandra	0.15
20m-Telescope	0.11
Keck II	0.11
VLT	0.054
ELT	0.028
GMT	0.008
Swift-XRT	0.007
Lynx	0.007
HST-WFC3	0.002
Athena	0.001

TABLE VI. Field-of-views (FOVs) for various electromagnetic telescopes.

A. Three-dimensional localization

The localization of the GW signal’s sky position is the key metric governing the feasibility of a follow-up with EM telescopes. Further, GW detections provide can provide more accurate distance measurement which are independent of cosmic ladder calibration issues and can help distinguish between a number of potential hosts. Finally, the visibility of certain EM phenomena such as gamma-ray bursts and jets depends on the binary’s orientation with respect to the observer’s line of sight. Thus, in this section we present the potential of the chosen networks to measure these metrics in form of the SNR, 90%-credible sky area, as well as luminosity distance and inclination angle errors for GW signals from redshifts $z \leq 0.5$.

Fig. 6 presents the distribution and correlation of SNR ρ , sky area Ω_{90} , and fractional luminosity distance error $\Delta D_L/D_L$ for BNS signals, with indications for the FOVs of various EM telescope, see Tab. VI, as well as the CDFs for all four metrics, including the absolute errors on the cosine of the inclination angle ι . We also summarize the expected detection rates of events with 90%-credible sky area $\Omega_{90}/\text{deg}^2 \leq 0.01, 0.1, 1$ and fractional luminosity distance errors $\Delta D_L/D_L \leq 0.01, 0.1$ in Tab. VII.

The cosmic merger rate for BNSs up to redshift $z = 0.5$ is approximately 12,000 per year. The top part of Fig. 6 and Tab. VII indicate that networks containing less than two *distinct* 3G detector sites will localize only a small fraction of these mergers per year, $\mathcal{O}(1)$ (HLVKI+) or $\mathcal{O}(10)$ (VK+HLIv, HLKI+E, and VKI+C), to within $\Omega_{90} \leq 0.1 \text{ deg}^2$, with the latter three observing a *handful* BNS mergers per year with $\Omega_{90} \leq 0.01 \text{ deg}^2$. Luminosity distances should be measured to better than 10% accuracy $\mathcal{O}(10)$ (HLVKI+, VK+HLIv), $\mathcal{O}(10^2)$ (VKI+C), and $\mathcal{O}(10^3)$ (HLKI+E) times per year; and only HLKI+E will be capable to observe a *few* events per year to sub-1% accuracy. The discrep-

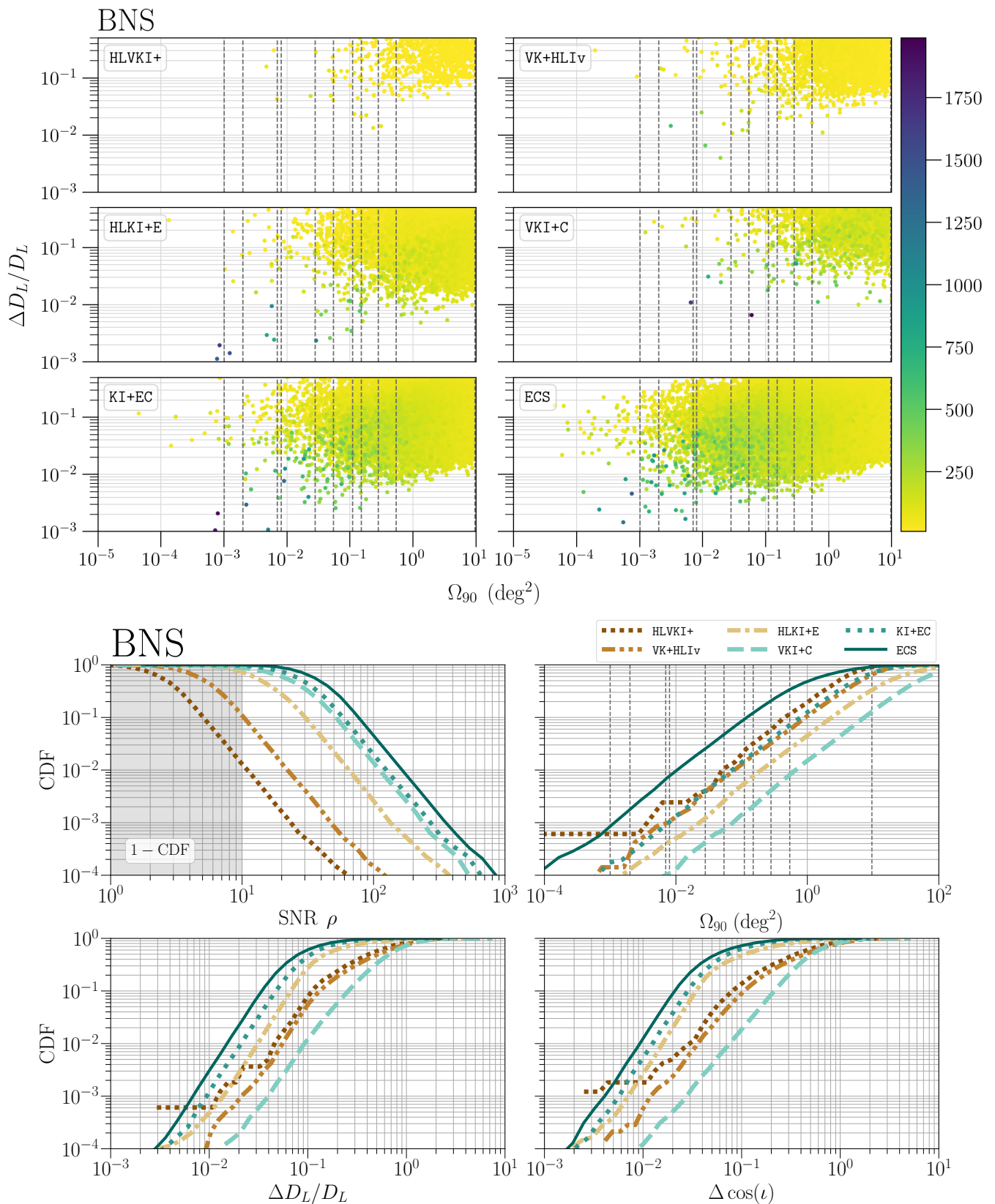


FIG. 6. *Top:* The scatter plots illustrate the correlations between SNR ρ , 90%-credible sky area Ω_{90} , and fractional luminosity distance error $\Delta D_L / D_L$ for BNS mergers with SNR $\rho \geq 10$ in the six studied A+, Voyager and 3G networks for redshifts $z \leq 0.5$. The color bar indicates the SNR of the events. The plots were generated from injections corresponding to an observation time of **10 years**.

Bottom: Cumulative density function (CDF) for the SNR ρ , 90%-credible sky area Ω_{90} , fractional luminosity distance errors $\Delta D_L / D_L$, and absolute errors on the cosine of the inclination angle $\Delta \cos(\iota)$ for BNS mergers observed in the six studied A+, Voyager and 3G networks for redshifts $z \leq 0.5$. The non-SNR panels are obtained for events with SNR $\rho \geq 10$, indicated by the non-shaded region in the SNR panel. The SNR CDF is flipped to highlight the behavior for large values.

Both: The dashed vertical lines in the Ω_{90} panels indicate the FOVs of the EM telescopes specified in Tab. VI.

ancy between the 3G networks HLKI+E and VKI+C stems from the sub-10 Hz sensitivity of ET and its ability to measure both polarizations by itself. KI+EC and ECS with two and three 3G sites will determine the sky positions for $\mathcal{O}(10)$ and $\mathcal{O}(10^2)$ per year to $\leq 0.01 \text{ deg}^2$, respectively, with ECS detecting such an event once every 3 days. Both networks will also measure the luminosity distance of $\mathcal{O}(10)$ events per year to sub-1% accuracies. Finally, only ECS with three 3G sites will confidently observe a few events per years with both $\Omega_{90} \leq 0.01 \text{ deg}^2$ and $\Delta D_L/D_L \leq 0.01$, see the top of Fig. 6.

While BNS mergers are the headlight events for multi-messenger astronomy, sparked by GW170817 and expected EM counterparts, the EM follow-up of BBH coalescences is equally intriguing, especially since astrophysicists want to explore the unclear origins of the massive BBHs LIGO and Virgo have observed so far. As such, Fig. 7 and Tab. VII summarize the potential for multi-messenger astronomy with BBHs up to redshift of $z = 0.5$. With a cosmic rate of only 1,200 BBH mergers per year, all networks localize a **quarter to all** of these signals to within 1 deg^2 . Further, BBHs localized to within 0.1 deg^2 will be observed at least once every two weeks irrespective of the network, with KI+EC and ECS pushing the rates to more than once and twice a day, respectively. In fact, both networks can pinpoint BBHs to within 0.01 deg^2 once a week and even almost once a day! Similarly, all studied networks are capable of determining the luminosity distance of a **quarter to all** BBHs to 10% or less, while better than 1%-level accuracies are much rarer, $\mathcal{O}(1)$, without two 3G networks. Again, KI+EC and ECS will actually detect such an event about once a day. The strong difference between the BNS and BBH rates for the given measurement accuracies in HLVKI+ are a result of the network's vastly different redshift reaches for BNS ($z_r \approx 0.11$) and BBH ($z_r \approx 0.6$).

Hence, we can conclude that essentially all six networks will provide EM astronomers with many BNS and BBH mergers to follow-up. KI+EC and ECS in fact will elevate pretty much all BBHs and thousands of BNS mergers up to redshift $z = 0.5$ to this level and further even enable the follow-up of dark siren events—in the absence of an EM counterpart—on a daily basis! As such, GW170817-like follow-up campaigns could become common-place and increasingly more dependent on the EM telescopes' availability and slewing capabilities. We also want to stress that while the rates KI+EC and ECS enable could be deemed as unnecessarily high, in reality, not every GW event can be followed-up due to maintenance outages of EM telescope, conflicts with other observations, or the potential of objects covering the EM counterpart or the source galaxy amongst other things.

B. Early warning alerts

The EM follow-up campaign of the event GW170817 was successful in spite of the fact that the earliest observations took place many hours after the epoch of merger, thereby missing critical data from the fireball that would have been launched moments after the merger as evidenced by the detection of gamma ray bursts by the Fermi gamma ray observatory and the INTEGRAL satellite a mere 1.7 s after merger. The alert from LIGO and Virgo with the full 3D localization of the event

TABLE VII. Detection rates of BNS and BBH mergers up to redshift $z = 0.5$ to be observed by different detector networks each year with $\Omega_{90}/\text{deg}^2 \leq 1, 0.1, 0.01$ as well as $\Delta D_L/D_L \leq 0.1, 0.1$, where Ω_{90} is the 90%-credible sky area and D_L the luminosity distance. These detection rates are calculated for events with $\text{SNR } \rho \geq 10$. Due to uncertainty in the various quantities that go into the calculation these numbers are no more accurate than one or two significant figures. The bare detection rates, events with $\text{SNR } \rho \geq 10$, for BNSs and BBHs up to redshift $z = 0.5$ are $\sim 12,000 \text{ yr}^{-1}$ and $\sim 1,200 \text{ yr}^{-1}$, respectively.

Metric	$\Omega_{90} (\text{deg}^2)$			$\Delta D_L/D_L$	
	≤ 1	≤ 0.1	≤ 0.01	≤ 0.1	≤ 0.01
<i>BNS</i>					
HLVKI+	34	3	0	12	0
VK+HLIV	160	16	2	77	0
HLKI+E	360	40	4	2,200	3
VKI+C	140	13	1	120	0
KI+EC	1,200	160	15	4,900	11
ECS	5,600	920	97	6,900	31
<i>BBH</i>					
HLVKI+	280	36	4	290	0
VK+HLIV	490	83	10	560	3
HLKI+E	610	120	12	1,100	94
VKI+C	430	54	6	580	27
KI+EC	1,100	360	50	1,200	220
ECS	1,200	830	250	1,200	390

was delayed by a little over 4.5 hrs. Six groups reported optical observations carried out between 10.89 hrs and 11.57 hrs after the epoch of merger. During the third observing run, GW alerts have been sent out with a average latency of **10 minutes** and there is effort to reduce the latency to less than a minute. So far, GW170817 remains the only GW event with an EM counterpart.

a. Motivation for observing events at the onset of merger

From an astrophysical point of view, there are compelling reasons to begin observation right at the onset of merger but that would require sending alerts before the epoch of merger to allow EM telescopes to slew to the right part of the sky. Early X-ray observations could resolve the initial state of the merger remnant, namely if a hypermassive NS forms first before collapsing to BH or if the remnant directly collapses to a BH. Prompt optical and infrared observations could inform the nature of the dynamical ejecta and outflow, formation of the accretion disc and the onset of r-process nucleosynthesis. Radio observations could shed light on the magnetosphere interactions between the two NSs before merger and test the hypothesis that some fast radio bursts result in the aftermath of a BNS merger. As we shall argue below, it should be possible to send out alerts before the epoch of coalescence and efforts are underway to accomplish this during the fourth observing run of the LIGO and Virgo detectors.

b. Coalescence time scale

Gravitational waves from the inspiral phase of BNSs last for tens of minutes to hours in ground-based detectors depending on the lower-frequency cut-off. The time left until coalescence, often referred to as *coales-*

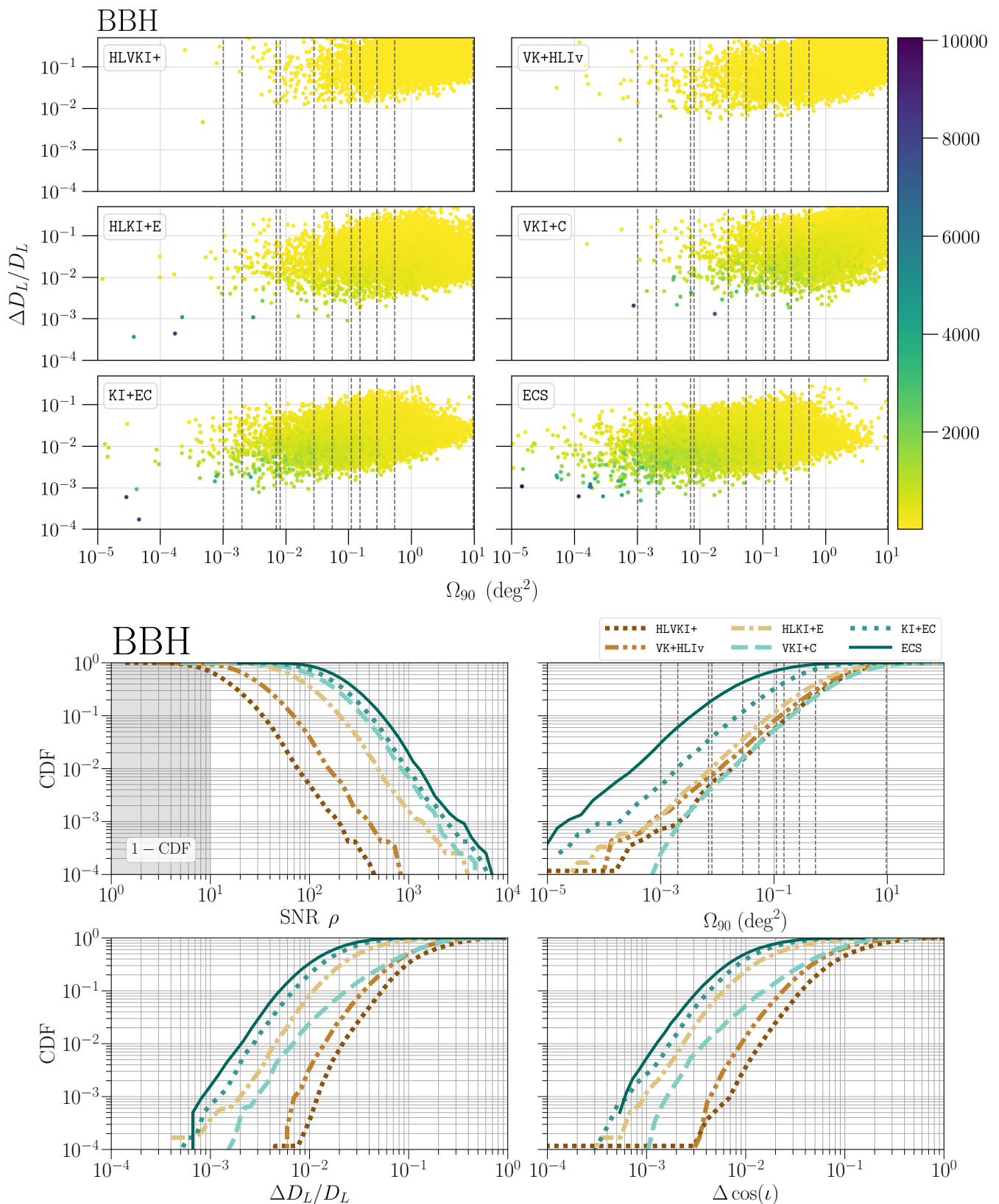


FIG. 7. *Top:* The scatter plots illustrate the correlations between SNR ρ , 90%-credible sky area Ω_{90} , and fractional luminosity distance error $\Delta D_L/D_L$ for BBH mergers with SNR $\rho \geq 10$ in the six studied A+, Voyager and 3G networks for redshifts $z \leq 0.5$. The color bar indicates the SNR of the events. The plots were generated from injections corresponding to an observation time of **10 years**.

Bottom: Cumulative density function (CDF) for the SNR ρ , 90%-credible sky area Ω_{90} , fractional luminosity distance errors $\Delta D_L/D_L$, and absolute errors on the cosine of the inclination angle $\Delta \cos(\iota)$ for BBH mergers observed in the six studied A+, Voyager and 3G networks for redshifts $z \leq 0.5$. The non-SNR panels are obtained for events with SNR $\rho \geq 10$, indicated by the non-shaded region in the SNR panel. The SNR CDF is flipped to highlight the behavior for large values.

Both: The dashed vertical lines in the Ω_{90} panels indicate the FOVs of the EM telescopes specified in Tab. VI.

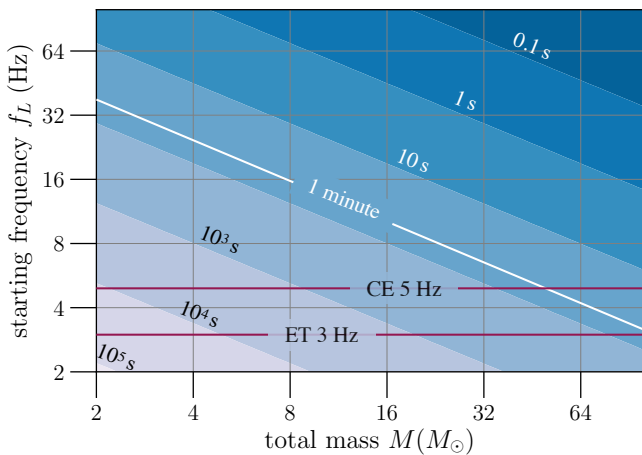


FIG. 8. The plot shows the duration (in seconds) for which a GW signal from an equal-mass binary of total mass M lasts until coalescence starting from frequency f_L .

cence time, starting from a frequency f_L , is given by

$$\tau \simeq \left(\frac{0.25}{\eta}\right) \left(\frac{2.8 M_\odot}{M}\right)^{5/3} \left(\frac{5 \text{ Hz}}{f_L}\right)^{8/3} 6.4 \times 10^3 \text{ s}, \quad (9)$$

where, as before, η is the symmetric mass ratio and M is the observed total mass of the system related to its intrinsic mass via $M \equiv (1+z)M_{\text{int}}$. Thus, asymmetric binaries last longer compared to symmetric ones but the time-scale is a sharp function of both the total mass and the starting frequency.

Figure 8 plots the duration of a compact binary signal as a function of the total mass and the starting frequency for equal mass (i.e., $\eta = 1/4$) binaries. In current detectors the lower-frequency cutoff is $f_L = 20$ Hz and sources are detected at $z \ll 1$. Thus, a typical BNS would last for a few minutes. With A+ detectors, which are expected to have a lower-frequency cutoff 10 Hz, this increases to about 15 minutes. For CE, however, a lower-frequency cutoff of 5 Hz is appropriate and BNSs at $z = 0$ would last for slightly less than two hours, while in the case ET $f_L = 3$ Hz is more appropriate in which case $\tau \sim 6.9$ hrs.

Thus, as a detector's low-frequency sensitivity improves signals last longer and some could be even be identified well before the epoch of coalescence, making it possible to send *early warning* (EW) alerts to EM telescopes to observe the events right at the onset of coalescence. Due to the sharp dependence of the time-scale on the total mass, it is far more plausible to send EW alerts for lower-mass systems than it is to do so for higher-mass binaries.

c. Early warning and localization Current algorithms are able to filter the data through a template bank within about 30 s after data acquisition. This includes time required for data transfer and application of denoising algorithms. With lower frequencies and longer duration templates filtering the data could take longer and we assume a latency of 60 s for data processing. To slew telescopes to the direction would also involve some latency and we assume that with automation this would be as low as 60 s. In what follows we will consider three EW times: $\tau_{\text{EW}} = 600$ s, $\tau_{\text{EW}} = 300$ s and $\tau_{\text{EW}} = 120$ s before merger. Given the EW time Eq. (10) can be inverted to

determine the frequency f_{EW} from which the system has time τ_{EW} left until coalescence:

$$f_{\text{EW}} \simeq \left(\frac{0.25}{\eta}\right)^{3/8} \left(\frac{2.8 M_\odot}{M}\right)^{5/8} \left(\frac{120 \text{ s}}{\tau_{\text{EW}}}\right)^{3/8} 22.2 \text{ Hz} \quad (10)$$

In computing the Fisher matrix integrals for EW alerts, we use a lower frequency of $f_L = 5$ Hz for all detectors except Virgo+ for which it is set to be $f_L = 10$ Hz (see Sec. II C) and an upper frequency cutoff of $f_U = f_{\text{EW}}$.

In order to follow-up GW events, EM telescopes would need to be given the 3D localization of the events with a fairly good accuracy. The best optical and infrared telescopes, such as the Rubin Observatory, have a FOV of 10 deg^2 , while others have narrower FOV of $\sim 1 \text{ deg}^2$. X-ray and radio observatories have still narrower FOV of $\sim 10^{-2} \text{ deg}^2$. We will, therefore, consider the number of events that can be localized to within $\Omega_{90} = 10 \text{ deg}^2$, 1 deg^2 and 0.1 deg^2 .

Most of the events observed by GW observatories cannot be localized to such a narrow region in the sky even with the full signal. However, 3G networks will have the ability to generate early warning alerts with good localization accuracy for a small fraction of BNS events from 2 to 10 minutes before the epoch of coalescence.

Figure 9 plots the cumulative density plots of the SNR (left panels) and Ω_{90} (right panels) for the detector networks considered in this study and BNS sources up to a redshift of 0.5. Less than 0.4% of events can be detected 2 minutes before coalescence in the case of the Voyager network. This number increases to **66% (54%)** for the VKI+C (HLKI+E) network and **95% (89%)** for ECS (KI+EC). In fact, ECS (KI+EC) could detect **88% (76%)** of the sources 5 minutes and **52% (34%)** 10 minutes before merger, respectively, while the corresponding numbers for VKI+C (HLKI+E) are **48% (47%)** and **5% (19%)**.

Tab. VIII lists the number of BNS events within a redshift of 0.5 that can be localized each year to within Ω_{90} of (10, 1, 0.1) deg^2 . We have left out HLVKI+ and VK+HLIv networks as they do not have any significant number of detections with the required sky localization at least 2 minutes before coalescence. The VKI+C network can only meet the requirement of good sky localization for a handful of events two minutes before merger.

From Tab. VIII, it is clear that ET plays a crucial role in the localization of events. The HLKI+E network is able to localize sources to within 10 deg^2 2 and 5 minutes before merger once a week or once every other week, respectively, while KI+EC and ECS detectors can do so for a few to several events every day. Thus, optical and infrared telescopes such as the Rubin observatory will have plenty of opportunity to observe mergers as they happen.

These numbers decrease by an order of magnitude for $\Omega_{90} \leq 1 \text{ deg}^2$, yet 3G observatories of KI+EC and ECS meet this constraints for hundreds of events each year, thereby providing ample number of events for early observation by EUCLID, WFIRST, Chandra 20 m Telescope and Keck II. The smaller FOV of optical and infrared telescopes, such as the VLT, ELT, and GMT, would require $\Omega_{90} \leq 0.1 \text{ deg}^2$ which will be met by roughly one event each month up to 5 min before the merger.

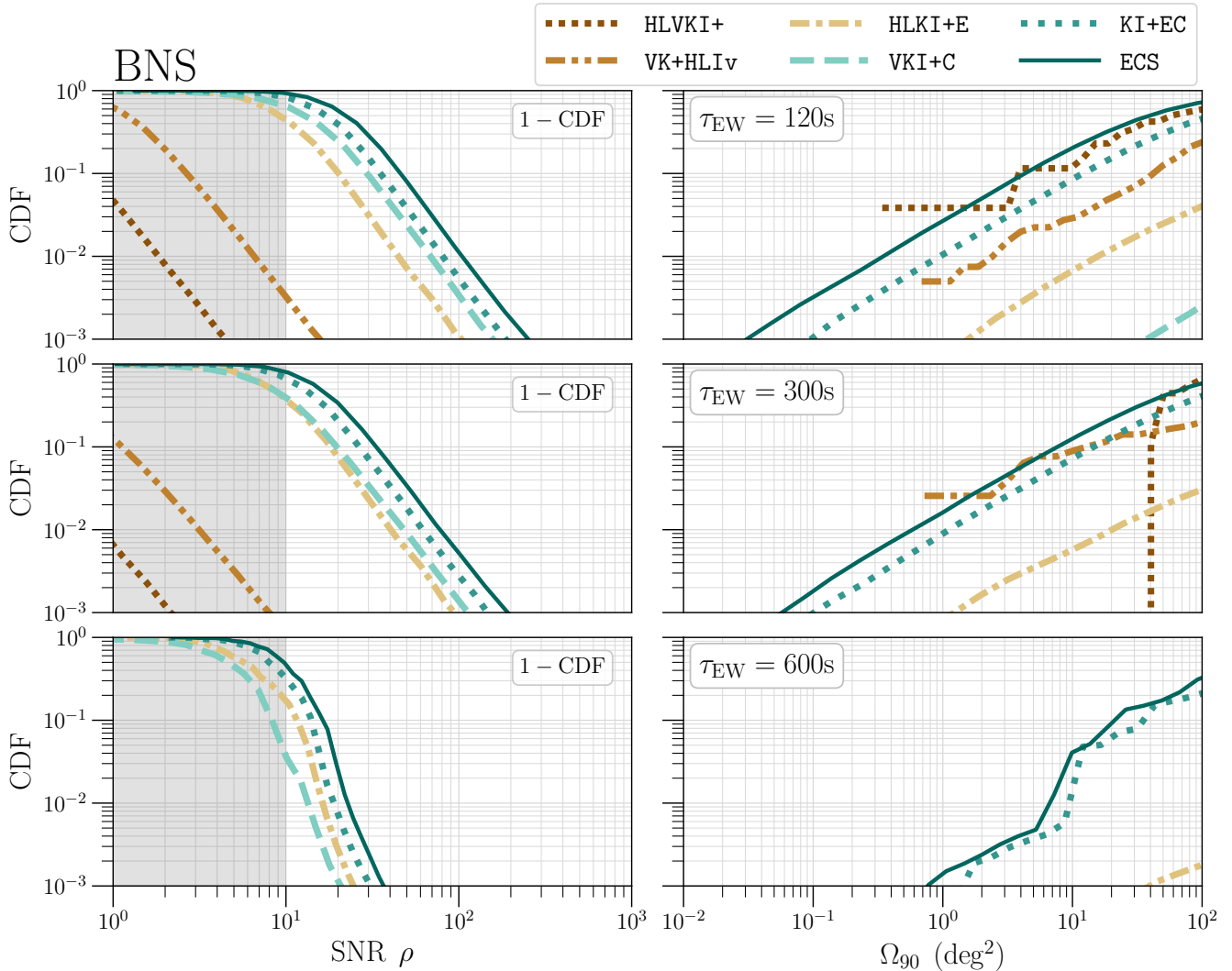


FIG. 9. The 3G networks will facilitate observation of the early onset of BNS mergers by a variety of different telescopes such as the Rubin observatory, EUCLID, WFIRST, Chandra x-ray observatory, 20 m Telescope, Keck II, VLT, ELT, GMT. The figure shows the cumulative histogram of the fraction of BNS events within a redshift of 0.5 as a function of SNR (left) and sky resolution (right) 2 minutes, 5 minutes and 10 minutes before merger. The 3G networks of KI+EC, and ECS will be able to detect $\geq 90\%$ of the events 2 minutes before merger localize 10% and 20% of all events within 10 deg^2 . ET with A+ array of detectors can provide tens of events within the same localization but a single CE with the A+ will only provide a handful of early warning alerts.

EW time	$\tau_{\text{EW}} = 120 \text{ s}$			$\tau_{\text{EW}} = 300 \text{ s}$			$\tau_{\text{EW}} = 600 \text{ s}$		
	≤ 10	≤ 1	≤ 0.1	≤ 10	≤ 1	≤ 0.1	≤ 10	≤ 1	≤ 0.1
HLKI+E	40	4	1	27	4	1	0	0	0
VKI+C	2	0	0	1	0	0	0	0	0
KI+EC	890	100	9	540	73	8	54	1	0
ECS	2,100	250	34	1,100	160	15	250	7	0

TABLE VIII. Number of events in different networks that can be localized to within a small region over the sky 2 minutes, 5 minutes and 10 minutes before merger. For a given early warning time τ_{EW} we determine the corresponding starting frequency f_{EW} using Eq. (10). The HLVKI+ and VK+HLIv networks do not meet the requirement of angular resolution for any of the early warning times considered.

VI. RARE AND LOUD EVENTS

The quality of science delivered by a GW network is determined by a combination of a large number of events at moderate SNR and a population of loud events, even if a small number, that would be useful in obtaining answers to certain key physics questions. The Advanced LIGO and Virgo network makes most of its observations at or near the threshold SNR [6, 7]. The loudest event so far is the BNS merger GW170817 [8] and it has undoubtedly delivered the best science to date, impacting many branches in physics and astronomy [10, 19, 22, 24, 25, 28, 31, 36]. The number of events observed until now is also low—about one per week [7]. As shown in Sec. IV, with the HLVKI+ network the number of BNS (BBH) events will increase to 100s (1000s) per year but there will not be (m)any high fidelity BNS or BBH signals with SNR well beyond 100. This is because, the number of events at an SNR of ρ_2 (300 or 1000), relative to an SNR of ρ_1 (100), would be roughly a factor $(\rho_2/\rho_1)^3$ (respectively, 27 or 1000) smaller. The VK+HLIV network will observe a handful of BBH events with SNR > 300 but not any high-SNR BNS mergers.

3G observatories will usher in an era of precision measurements by observing large populations of signals that are needed to mitigate statistical uncertainties and systematic biases for some of the inferences (e.g. precision cosmology); with thousands of high-SNR ($\rho \geq 300$) events that could help in detecting subtle signatures of new physics, e.g. dark matter, violation of general relativity (GR), etc. In this section we briefly discuss some of the most impactful science enabled by 3G observatories.

a. Understanding the nature of black holes BHs are unlike other macroscopic objects. Perturbed BHs return to their quiescent state by emitting GWs whose spectra is completely determined by the BH's mass and spin angular momentum via a theorem called the *black hole no-hair theorem* [85, 86]. Thus, by observing how the remnant of a compact binary coalescence settles down to its final state could tell us about its nature but to do so, it is necessary to observe not just the fundamental mode of the GW spectrum but the higher modes and overtones excited in the process of coalescence [87–89]. Unfortunately, the amplitude of the sub-dominant modes and overtones is generally far lower than the dominant, fundamental quadrupole mode and detecting them would require high-SNR events [90–92]. For example, the loudest BBH event so far, GW150914, had an estimated SNR of between 4 to 8.5 in the ringdown part of the signal [17], depending on when the ringdown signal is assumed to begin, compared to an SNR of 24 in the full inspiral-merger-ringdown signal [3]. Thus, the ringdown signal alone was not loud enough to accurately measure the parameters of even the dominant mode. To test the black hole no-hair theorem one would need to measure the complex frequencies of at least two modes with the SNR in weaker modes in excess of 15 to 20. This would require SNRs of several hundreds or more in the full signal (see, e.g., Fig. 1 of Ref. [89]) which is only accessible to 3G observatories (cf. Tab. IV).

In addition to testing the no-hair theorem with perturbed BHs, it is possible to test GR by checking the consistency of the binary parameters estimated using different multipoles provided there is enough SNR from higher order modes [93, 94]. For example, the octupole mode of the inspiral signal

from GW190814 is estimated to have an SNR of about 6.6 compared to the total SNR of 21.4 in the full signal [16].

b. Inferring dense matter equation of state and QCD phase transition Understanding the equation of state of dense nuclear matter is one of the open problems in fundamental physics (see, e.g. Ref. [95]). GW observations can determine an effective tidal deformability of a BNS system but not the tidal deformabilities of each of the companions [96, 97]. Inferring the radius of each companion would require additional assumptions that may not be valid [98, 99]. BNS mergers with SNRs in excess of several hundreds, which will be rare but abundant in the 3G era, will enable accurate inference of the tidal deformabilities of both NSs without requiring additional assumptions [100]. Thus, we expect 3G observatories to measure radii of NSs to within a few hundred meters and infer the equation of state of cold dense nuclear matter to a high degree of precision [72]. The post-merger oscillations could also carry the signature of dense matter equation of state that could be determined by 3G observatories by accurately measuring the complex oscillation frequencies [101–104].

The remnant that forms after the coalescence of a BNS could sometimes be a hypermassive NS with core densities possibly exceeding several times the nuclear density [105, 106]. At such densities, matter could undergo quark-deconfinement phase transitions [107], from the hadronic phase to quark-gluon plasma, and this signature would be present in the post-merger GWs emitted by the hypermassive remnant [108, 109]. 3G networks would observe post-merger signals with SNRs of 20 or more [?] depending on the equation-of-state and thereby shed light on the QCD (quantum chromodynamic) phase transition.

c. Testing general relativity GR is consistent with laboratory experiments and astronomical observations over a wide range of field strengths [110]. Yet, the theory raises a number of fundamental questions that have not found satisfactory answers [111, 112]. These include BH information loss [113] and non-unitary evolution of quantum states [114], the late-time accelerated expansion of the Universe and the nature of the cosmological constant or dark energy [115, 116], BH and big bang singularities that pose a major conceptual hurdle in predictability [117], to name a few. By directly probing BH horizons and the way remnant objects approach their final state it will be possible to probe predictions of GR to higher precision [88]. 3G observatories with thousands of high-SNR events with SNR > 300 will not only detect many subtle effects predicted in GR but allow precision tests of the theory [118]. For example, by measuring the final state of the BH and comparing it to the properties of the progenitor binary when the companion stars are widely separated it will be possible to test strong-field predictions in the full non-linear GR [119, 120]. Additionally, it will be possible to test predictions of alternative gravity theories invoked to explain the Universe's recent (i.e. $z \lesssim 1$) accelerated expansion, the presence of dipole radiation, and constraints on the Brans-Dicke parameter [121, 122]. With signals that arrive from very large redshifts ($z \gtrsim 10$) it will be possible to set tighter bounds on the graviton mass [123] and Lorentz violations [124].

VII. CONCLUSION

A. Summary of results

a. Visibility of full cosmic populations Due to the vastly different reaches, see Fig. 2, the visibility of BNS mergers differs vastly between the three generations, see Tab. IV. These range from detections of $\rho \geq 10$ -events every other day with A+ over $\rho \geq 30$ -events once a week with Voyager to daily BNS signals with $\text{SNR } \rho \geq 100$ in 3G networks containing a CE detector. The lower sensitivity of ET results in less frequent detections, once every two weeks, of such loud BNS events in HLKI+E.

Since all networks have farther reaches for BBHs signals, the BBH detection rates outpace the BNS in the networks without a CE detector—yielding two $\rho \geq 30$ -events every three days with A+, weekly $\rho \geq 100$ -events with Voyager, and almost six $\rho \geq 100$ -events per day with ET—while the rates of networks containing a CE detector are bound by the cosmic merger rate, *CE networks will observe nearly all BBHs up to redshift $z = 10$* . These networks, containing either one CE, one CE and ET, or two CEs and one ET, will observe about 20 to 50 BBH signals with $\rho \geq 100$ per day. As such the differences in other metrics are discriminating factors for BBH detections.

b. Measurement quality - three-dimensional localization While the sky localization and distance estimation metrics generally follow the tendencies of the networks' visibility metric, see Tab. V, there are two stark exceptions. The 3G networks containing either only one CE or only one ET exchange their roles: while ET has a lower sensitivity for BNS and BBH mergers than that of CE, its low-frequency sensitivity and geometry are very advantageous for sky localization and also distance estimation.

Hence we can expect the following sky localization rates for BNS mergers from the examined networks: The A+ detector network will only observe confidently events to within $\Omega_{90} \leq 1 \text{ deg}^2$ every other week. Both VK+HLIv and VKI+C should deliver similar rates of BNS mergers localized to within $\Omega_{90} \leq 0.1 \text{ deg}^2$, while HLKI+E will push this number to once a week. Sky localizations of BNS events better than $\Omega_{90} \leq 0.01 \text{ deg}^2$ will only be achieved with two or three 3G detectors in the network: KI+EC and ECS will detect such high-fidelity events every other week to four times a week.

While coalescences of BNSs are expected to be more abundant compared to BBHs, the intrinsic loudness of BBH mergers increases the detection rates of well-localized events: A+ networks will localize one event per week to within $\Omega_{90} \leq 0.1 \text{ deg}^2$ while Voyager and single CE networks push the rate to almost five per week. In fact both networks will localize BBHs to within $\Omega_{90} \leq 0.01 \text{ deg}^2$ about every third week, with the ET-only network reaching weekly rates at such sky localizations. Networks with two and three 3G detectors will observe such well-localized events four times a week (KI+EC) or up to four times per day (ECS)! Thus, while the visibility did not allow for conclusive discrimination of the networks containing a CE detector, the sky resolution clearly favors those with at least two, preferably three 3G detectors.

Finally, luminosity distance estimation accuracies better than 10% show a wide range for BNS mergers: few per year with A+, twice a week with Voyager, seven times per day with

one ET, three times a week with one CE, and 30 to 100 times per day in KI+EC and ECS, respectively. BBH signals will push these numbers to twice a day with A+, 10 times a day with Voyager, and at least 30 times per day in 3G networks. In fact such networks will detect BBHs to sub-1% accuracies in the luminosity distance once a week with one CE and up to five times a day with three 3G detectors.

c. Enabling multi-messenger astronomy The synergy of GW and EM observations was beautifully demonstrated with the GW170817 event. As such each network's potential to enable a follow-up in the EM spectrum—even without the detection of a loud EM transient such as a GRB—is paramount in determining the network's science capabilities. The main metric is thus the sky localization in relation to the FOVs of various EM telescopes, see Tab. VI. We performed this study for BNS and BBH signals emitted from redshifts up to $z = 0.05$.

An A+ network will observe BNS about once every other week with a 90%-credible sky area of $\Omega_{90} \leq 1 \text{ deg}^2$ and thus predominantly cater to the Rubin Observatory for follow-up surveys. Voyager and single 3G detector networks should localize BNS events to within 0.1 deg^2 10 to 40 times a year, thus enabling EM surveys with the EUCLID, WFIRST, Chandra, Keck II, and the 20m-Telescope. A CE-ET network would see such events every other day and extremely well-localized signals with $\Omega_{90} \leq 0.01 \text{ deg}^2$ once every four weeks. The latter would make follow-ups with the VLT and ELT feasible. A triple-3G network will observe $\Omega_{90} \leq 0.01 \text{ deg}^2$ -events about once every three days and potentially observe tens of BNS signals to within 0.001 deg^2 , see the top of Fig. 6. With such accuracy even GMT, Swift-XRT, Lynx, HST-WFC3, and Athena could serve as EM follow-up telescopes. In fact, the triple-3G network is the only network to observe consistently BNS mergers that are well-localized both on the sky ($\Omega_{90} \leq 0.01 \text{ deg}^2$) and in distance ($\Delta D_L/D_L < 0.01$), see Fig. 6.

BBH detections lack EM counterparts and therefore depend on the sky localization from the GW signal to identify the binary's host galaxy. Fortunately, the intrinsic loudness of massive systems and the signal contributions from higher modes for mass-asymmetric binaries improve the sky localization estimates across all six networks, allowing them to localize BBH signals to within 0.1 deg^2 on at least a bi-weekly basis. Thus, frequent EM follow-up surveys are possible with the following telescopes: Rubin Observatory, EUCLID, WFIRST, Chandra, Keck II, and the 20m-Telescope. In fact the CE-ET and triple-3G networks will observe such well-localized more than once or twice a day. They will further provide VLT and ELT with $\Omega_{90} \leq 0.01 \text{ deg}^2$ -events once a week or even once every other day. These networks will consistently measure the three-dimensional localization of tens of BBHs events to better than $\Omega_{90} \leq 0.001 \text{ deg}^2$ and $\Delta D_L/D_L < 0.01$ allowing for follow-up surveys by GMT, Swift-XRT, Lynx, HST-WFC3, and Athena and enabling single-event, high-precision cosmology with dark sirens [77].

One particularly intriguing aspect of multi-messenger astronomy with GWs and EM radiation is the potential to trigger EW alerts for BNS coalescences ahead of the actual merger, thus enabling the EM observatories to record the events as early as possible and observe the merger in the EM spectrum as it

happens. The important metric here, besides visibility, is the sky localization of the events several minutes before the merger to provide enough time for GW signal processing to issue an alert and telescopes to slew to the estimated sky location. In our study we found that A+ and Voyager detectors will not provide such significant detection rates with the requires sky localization at least 2 minutes before the merger. Similarly, a single CE network might only observe a couple such events per year early enough for the Rubin Observatory to follow-up. In contrast, the ET network should send 2 min alerts weekly and up to 10 min alerts bi-weekly. The CE-ET and triple-3G network on the hand will push these number to 10 daily 2 min and 3 daily 10 min alerts to the Rubin Observatory. In fact, both networks would even provide EUCLID, WFIRST, Chandra, Keck II, and the 20m–Telescope with 2 min and 10 min EW alerts for a handful of events per year, see Tab. VIII.

B. Limitations of the study

The main caveat of this study is the use of the Fisher information formalism to provide measurement quality estimates. The formalism is well-known and tested, but can only provide estimates for Gaussian posteriors which is likely not the best assumption for the noise of these detectors; especially for signals at visibility threshold. Further, the reliance on numerical derivatives for LAL waveforms and the numerical inversion of the Fisher matrix are sources for numerical uncertainties affecting the quoted results. Further, we did not examine the quality of spin measurements since the addition of such paramters in the Fisher analysis lead to a high rate of ill-conditioned Fisher matrices for which the numerical inversion is not to be trusted.

Further, the chosen population distributions—chosen to be consistent with the LIGO and Virgo observations both in mass and redshift distributions—do not capture unexpected sources such large merger population of population III star remnants or primordial BHs at large redshifts beyond $z = 10$. Besides, we did not include the effects of precession in the examined waveforms and populations.

C. Outlook and further studies

Ultimately we can conclude that while the A+ and Voyager upgrades would do a tremendous job to increase the current detector facilities' lifespan and science capabilities. Yet, only two- and three-site 3G networks will expand the detection reach significantly to observe binary black hole mergers from the edge of the observable Universe; a regime inaccessible to electromagnetic observations. These networks would be capable to observe most binary coalescences up to medium redshifts and thus provide abundant detection rates enabling scientists to examine binary progenitor population and formation channels, map the large-scale structure of the universe, perform high-precision cosmology and tests of GR, etc. Further, the three-dimensional localization capabilities of such networks should enable a host of electromagnetic telescopes to not only follow-up the detections searching for counterparts and host galaxies, but actually even alert these observatories

minutes before the actual mergers in the case of BNSs, allowing astronomers to record the mergers in the electromagnetic spectrum as it happens. Finally, the large rates would further provide redundancies for follow-up surveys to ensure that enough gravitational-wave events can be examined in the electromagnetic window when accounting for maintenance and already reserved observation time.

The planned and proposed detector updates and new facilities will be an important addition for the fundamental physics, astrophysics and cosmology communities.

ACKNOWLEDGMENTS

We thank members of the Cosmic Explorer project team, in particular Stefan Ballmer, Matthew Evans, Anuradha Gupta, Evan Hall, Kevin Kuns, Philippe Landry, Geoffrey Lovelace, Jocelyn Read, Josh Smith, Salvatore Vitale, (add everyone else that helped with noise curves, science, etc.) for many helpful conversations.

Appendix A: Visibility: Detection Efficiency Fits and Probability Density Functions

In Sec. IV we presented the cumulative density plots of the SNR, 90%-credible sky area, and other parameters. Here we show the corresponding probability density functions for the respective parameters. Figs. 10 and 11 shows the probability density functions on a log-log scale. Since the total number of events accessible each year is in excess of a million for BNS and more than one-hundred thousand for BBH, we have shown the probability density functions over five orders of magnitude in density. This will help recognize events at the tail end of the distribution that cannot be easily inferred from the cumulative distribution. In order to minimize Monte Carlo errors we have used a number of events expected over a 10-year period. However, as discussed in Sec. IV, numbers quoted in the text and various tables assume a 1-year observation period.

While events at the tail end of the distribution are rare, they would be very loud and their parameters will be measured with great precision. For example, only 3G observatories have the potential to observe significant number of BNS (BBH) mergers with SNRs larger than 100 (1000) and localize sources to better than 10 arc min^2 . We examine the science potential of these tail ends events in Sec. VI.

The density plots readily reveal the mode of the distributions, indicating where to expect most of the events to lie, and limitations of different networks, informing the best science return we can hope to extract. In fact, we see that the three generations (A+, Voyager, and 3G) are qualitatively different with respect to every metric used in this study.

Appendix B: Cosmic Explorer: Influence of Proposed Detector Configurations

In developing the science case for a 3G GW detector proposal, the Cosmic Explorer Project is investigating various configurations of CE detectors, e.g. with varying de-

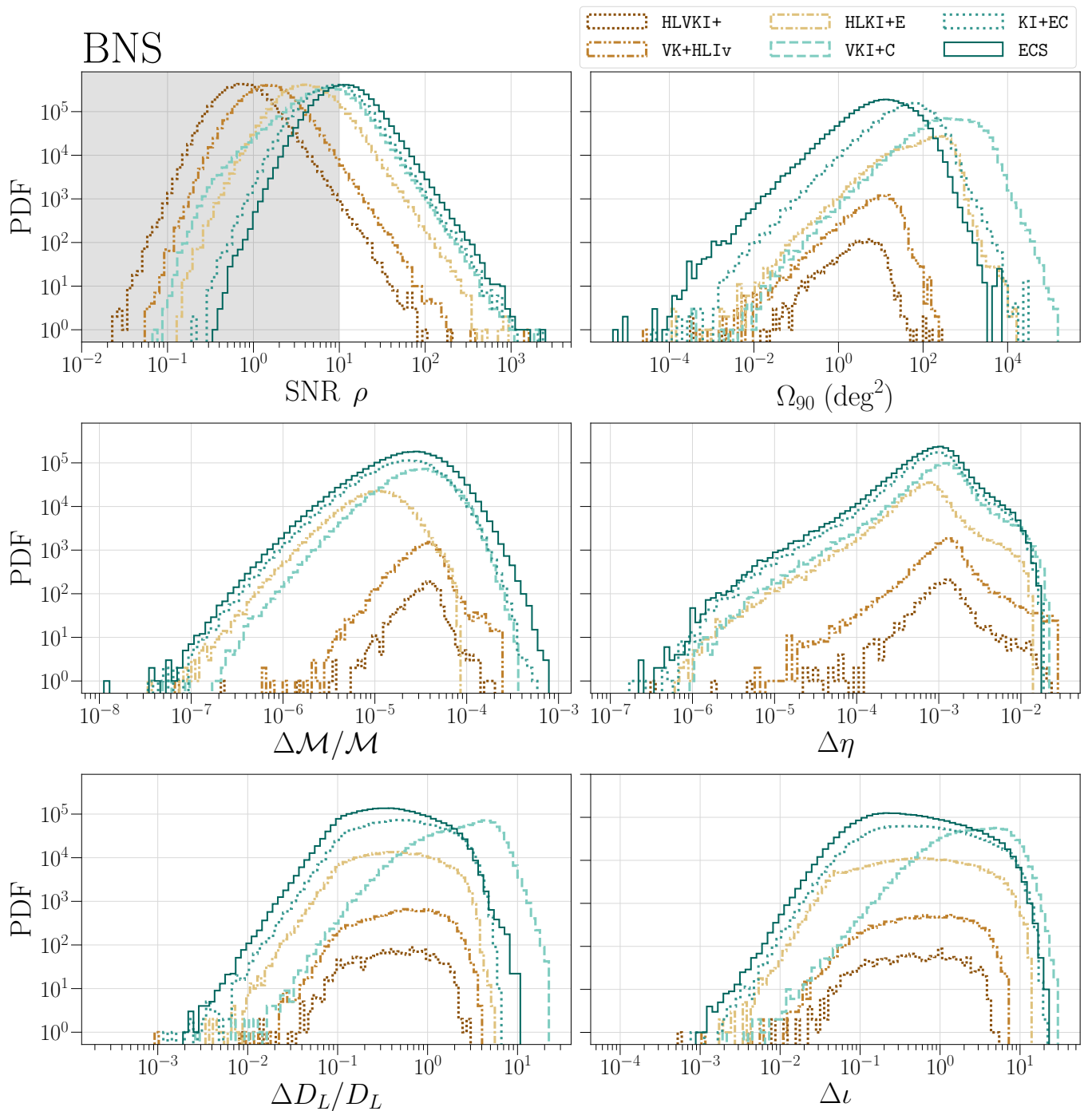


FIG. 10. Histograms of the **10 years** BNS injection sample used to generate Fig. 3 for SNR ρ , 90%-credible sky area Ω_{90} , fractional errors on chirp mass $\Delta M/M$ and luminosity distance $\Delta D_L/D_L$, and absolute errors on symmetric mass ratio $\Delta \eta$ and cosine of the inclination angle $\Delta \cos(i)$ observed in the six studied A+, Voyager and 3G networks. The non-SNR panels are obtained for events with SNR $\rho \geq 10$, indicated by the non-shaded region in the SNR panel.

tector arm lengths and hence detectors sensitivity curves, see Fig. 12. Given the early state of the CE detector proposal, we included, for completeness, four networks containing one or two CE detectors with either 20 km or 40 km arms to demonstrate the potential of 3G networks without an ET detector: VKI+C..20, VKI+C..40, VKI+C..20-40, and VKI+C..40-40. The VKI+C..40 network is the same as VKI+C and is included as a reference from the main body of

this paper. Figs. 13 to 21 reiterate the plots presented throughout this paper for these four CE networks instead of the six studied A+, Voyager, and 3G networks.

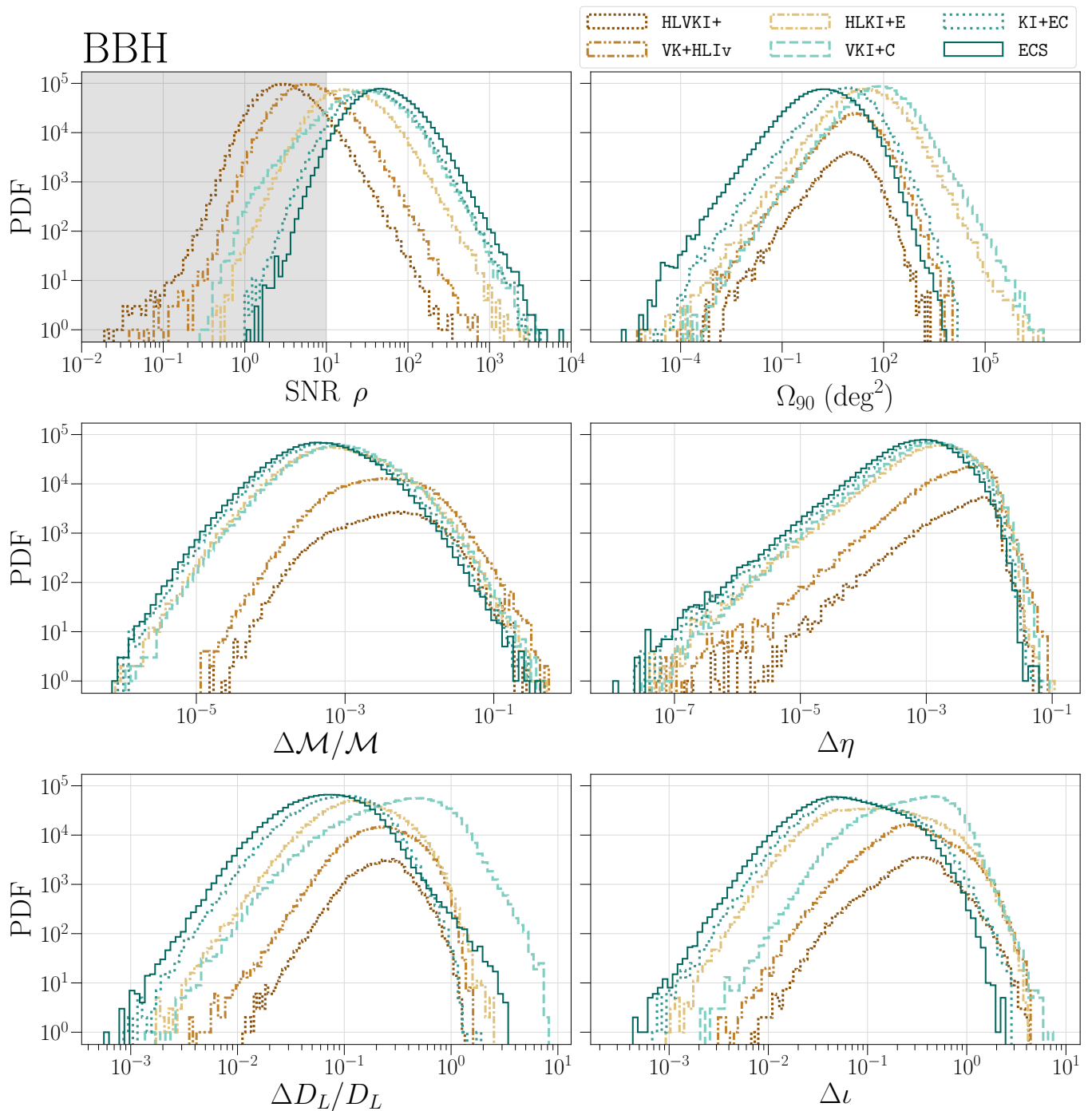


FIG. 11. Histograms of the **10 years** BBH injection sample used to generate Fig. 4 for SNR ρ , 90%-credible sky area Ω_{90} , fractional errors on chirpmass $\Delta M/M$ and luminosity distance $\Delta D_L/D_L$, and absolute errors on symmetric mass ratio $\Delta \eta$ and cosine of the inclination angle $\Delta \cos(i)$ observed in the six studied A+, Voyager and 3G networks. The non-SNR panels are obtained for events with SNR $\rho \geq 10$, indicated by the non-shaded region in the SNR panel.

Appendix C: gwBENCH settings

Tabs. IX and X record the best-fit parameters a , b , and c of the sigmoid curves fitted to the detector efficiencies $\epsilon(z)$ in Fig. 2 Sec. III and Fig. 13 in App. B, respectively.

Appendix D: gwBENCH settings

In gwbench we used numerical derivatives with the following settings: `step = 1e-9`, `method = 'central'`, `order = 2`, and `d_order_n = 1`. Further we set `use_rot = 1`, `conv_cos = ('dec', 'iota')`, `conv_log = ('Mc', 'DL', 'lam_t')`. The waveform models were

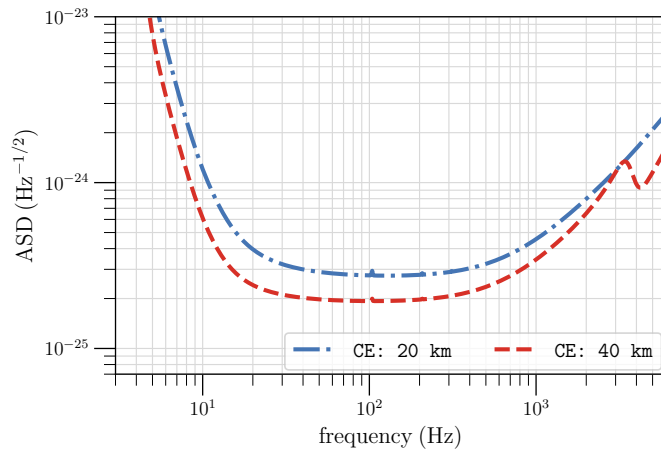


FIG. 12. Sensitivity of the two examined Cosmic Explorer configurations with 20 km and 40 km arm length, respectively. The noise curves are taken from the `ce2.20km.cb` and `ce2.40km.cb` .txt-files inside `ce_curves.zip` file at <https://dcc.cosmicexplorer.org/CE-T2000007>.

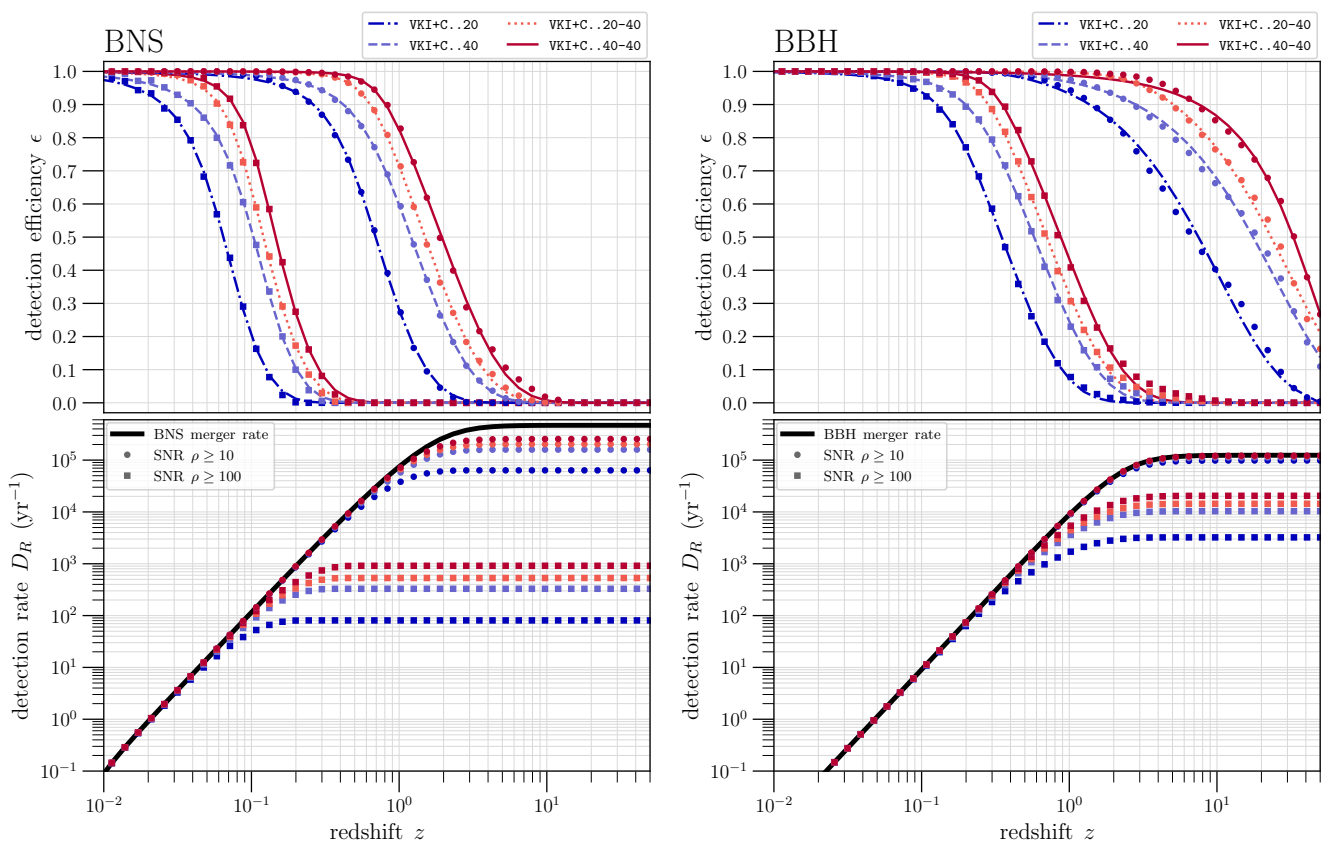


FIG. 13. Detection efficiencies ϵ and detection rates D_R of the four studied CE networks are plotted as functions of redshift z . The circles (squares) denote the values for events with $\text{SNR } \rho \geq 10$ ($\rho \geq 100$). The thick, black lines in the rate panels are the cosmic BNS and BBH merger rates, see Sec. III. The fit lines in the efficiency panels are sigmoid fits with $f_{\text{sigmoid}} = \left(\frac{1+b}{1+be^{ax}}\right)^c$.

```
wf_model_name = 'lal.bns',          wf_other_var_dic
= {'approximant': 'IMRPhenomD_NRTidalv2'} for
BNS injections and wf_model_name = 'lal.bbh',
wf_other_var_dic = {'approximant': 'IMRPhenomHM'}
for BBHs. The injection sets were generated
using the injections module of gwbench:
injections.injections_CBC.params.redshift with
```

```
redshifted = 1. For BNSs we used the following seeds for
the various redshift bins (zmin, zmax, seed): (0, 0.5, 7669),
(0.5, 1, 3103), (1, 2, 4431), (2, 4, 5526), (4, 10, 7035), and (10,
50, 2785). For BBHs we used (0, 0.5, 5485), (0.5, 1, 1054), (1,
2, 46), (2, 4, 5553), (4, 10, 5998), and (10, 50, 4743).
```

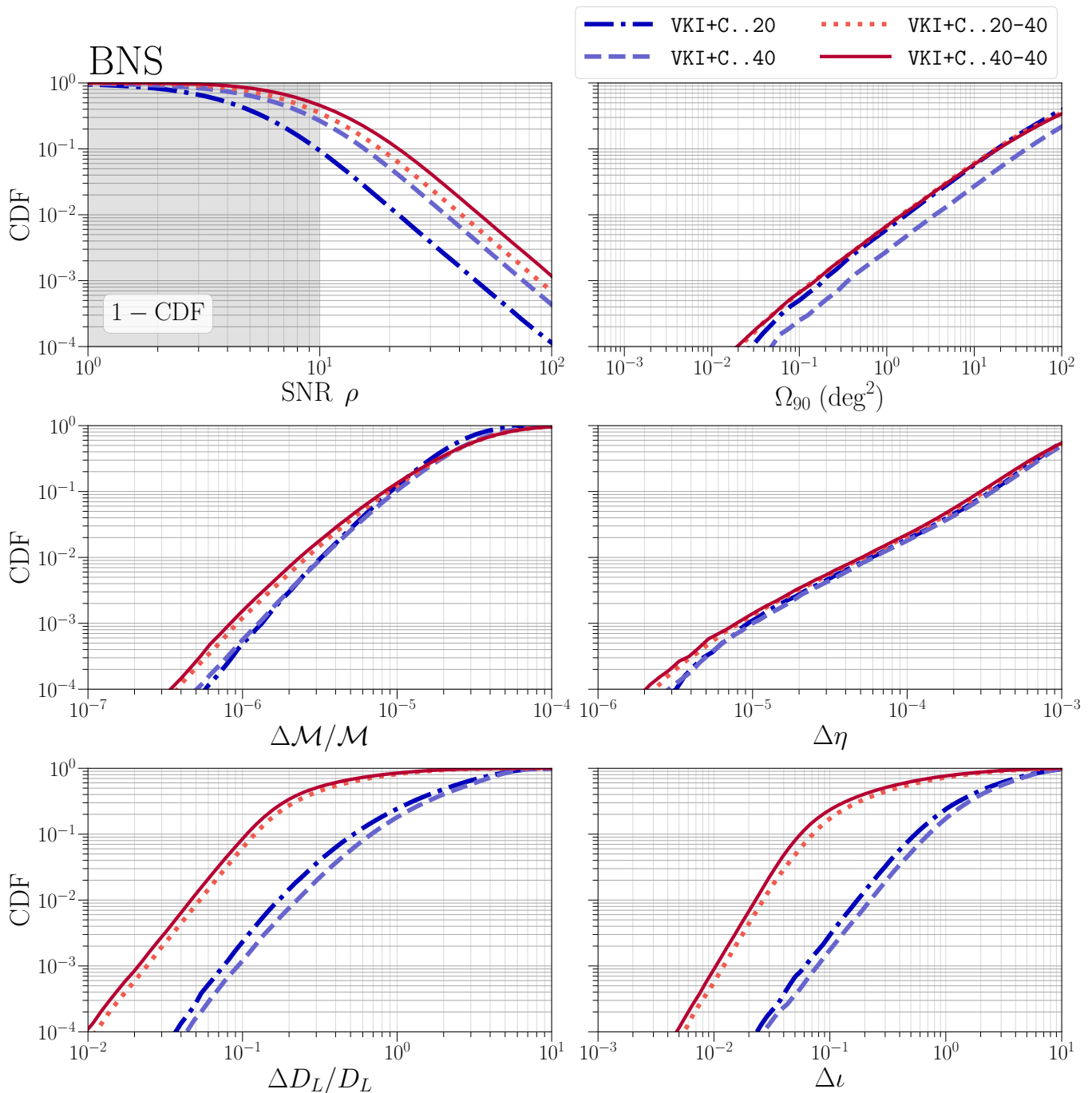


FIG. 14. Cumulative density function (CDF) for the SNR ρ , 90%-credible sky area Ω_{90} , fractional errors on chirp mass $\Delta M/M$ and luminosity distance $\Delta D_L/D_L$, and absolute errors on symmetric mass ratio $\Delta \eta$ and cosine of the inclination angle $\Delta \cos(\iota)$ for BNS mergers observed in the four studied CE networks. The non-SNR panels are obtained for events with SNR $\rho \geq 10$, indicated by the non-shaded region in the SNR panel. The SNR CDF is flipped to highlight the behavior for large values.

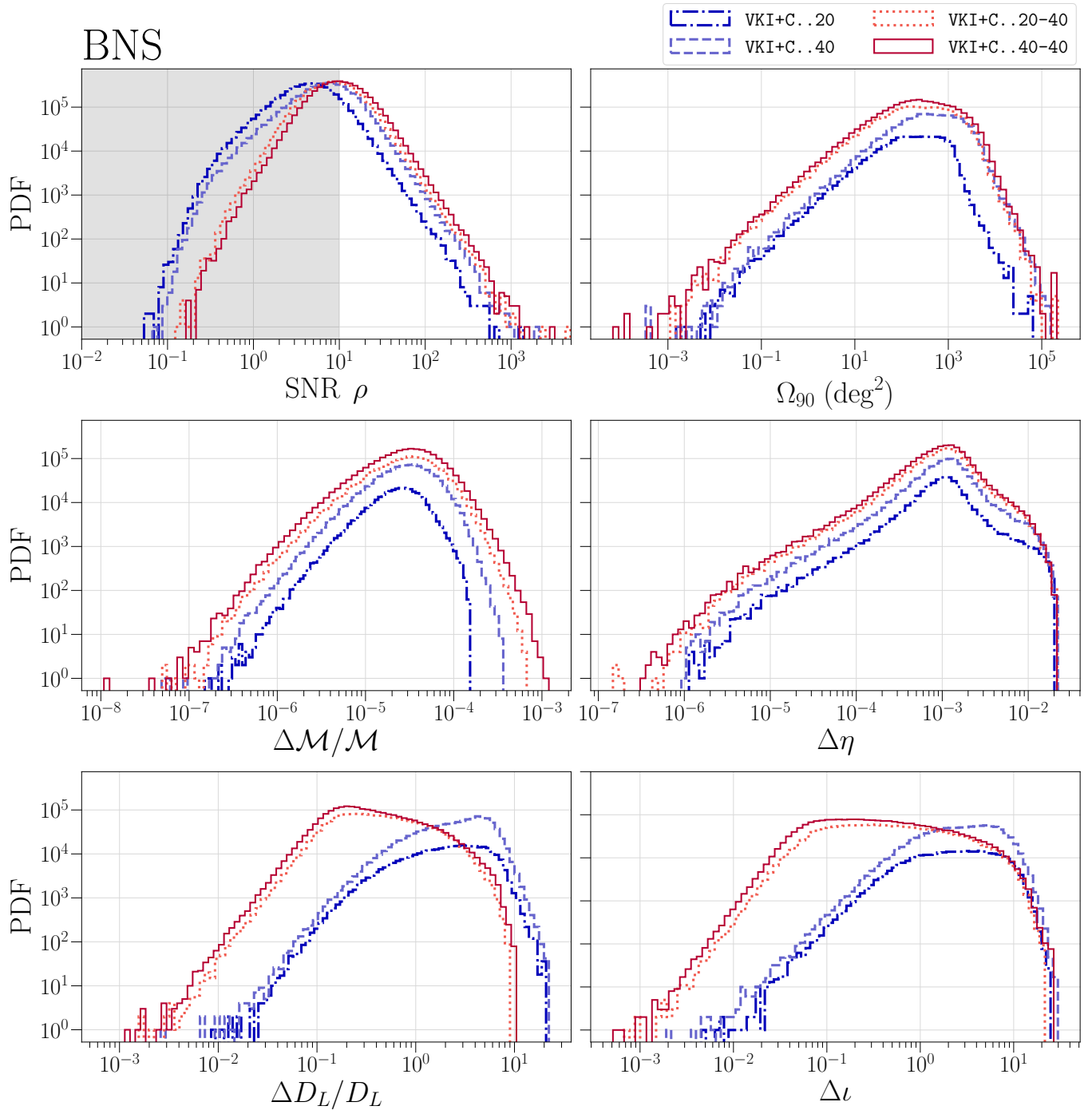


FIG. 15. Histograms of the **10 years** BNS injection sample used to generate Fig. 3 for SNR ρ , 90%-credible sky area Ω_{90} , fractional errors on chirpmass $\Delta\mathcal{M}/\mathcal{M}$ and luminosity distance $\Delta D_L/D_L$, and absolute errors on symmetric mass ratio $\Delta\eta$ and cosine of the inclination angle $\Delta\cos(\iota)$ observed in the four studied CE networks. The non-SNR panels are obtained for events with SNR $\rho \geq 10$, indicated by the non-shaded region in the SNR panel.

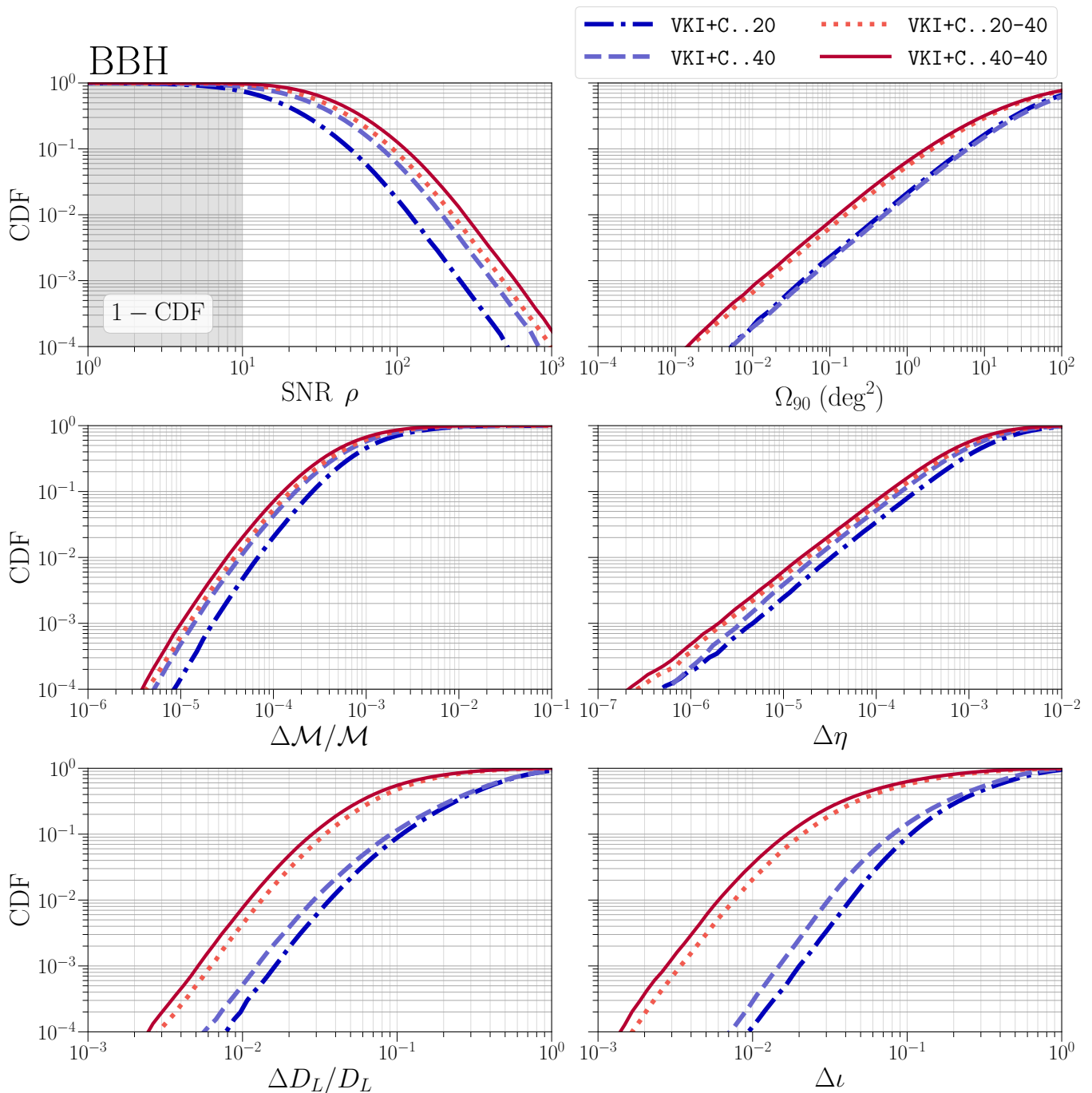


FIG. 16. Cumulative density function (CDF) for the SNR ρ , 90%-credible sky area Ω_{90} , fractional errors on chirp mass $\Delta\mathcal{M}/\mathcal{M}$ and luminosity distance $\Delta D_L/D_L$, and absolute errors on symmetric mass ratio $\Delta\eta$ and cosine of the inclination angle $\Delta\cos(i)$ for BBH mergers observed in the four studied CE networks. The non-SNR panels are obtained for events with SNR $\rho \geq 10$, indicated by the non-shaded region in the SNR panel. The SNR CDF is flipped to highlight the behavior for large values.

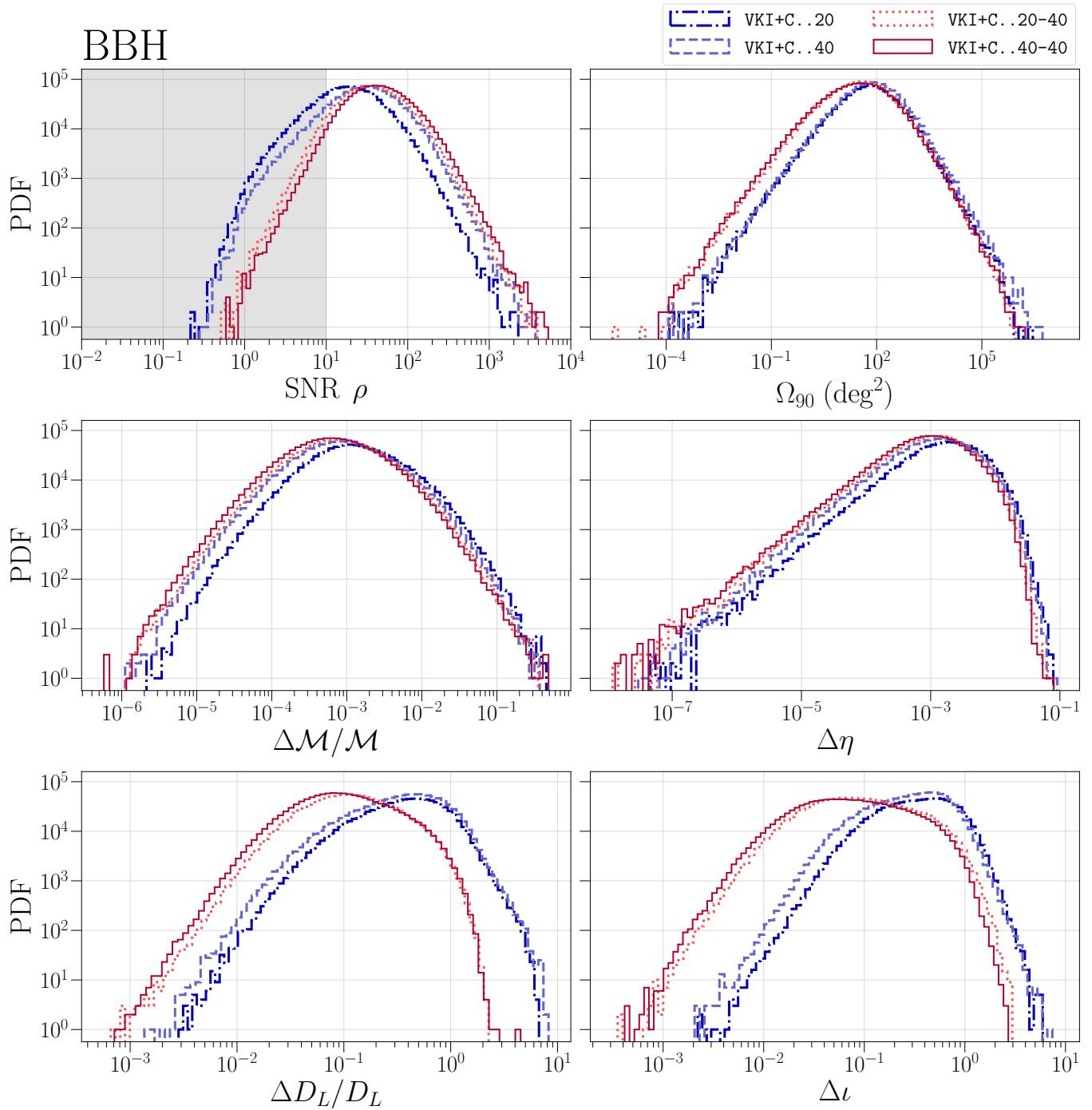


FIG. 17. Histograms of the **10 years** BBH injection sample used to generate Fig. 4 for SNR ρ , 90%-credible sky area Ω_{90} , fractional errors on chirpmass $\Delta \mathcal{M}/\mathcal{M}$ and luminosity distance $\Delta D_L/D_L$, and absolute errors on symmetric mass ratio $\Delta \eta$ and cosine of the inclination angle $\Delta \cos(\iota)$ observed in the four studied CE networks. The non-SNR panels are obtained for events with SNR $\rho \geq 10$, indicated by the non-shaded region in the SNR panel.

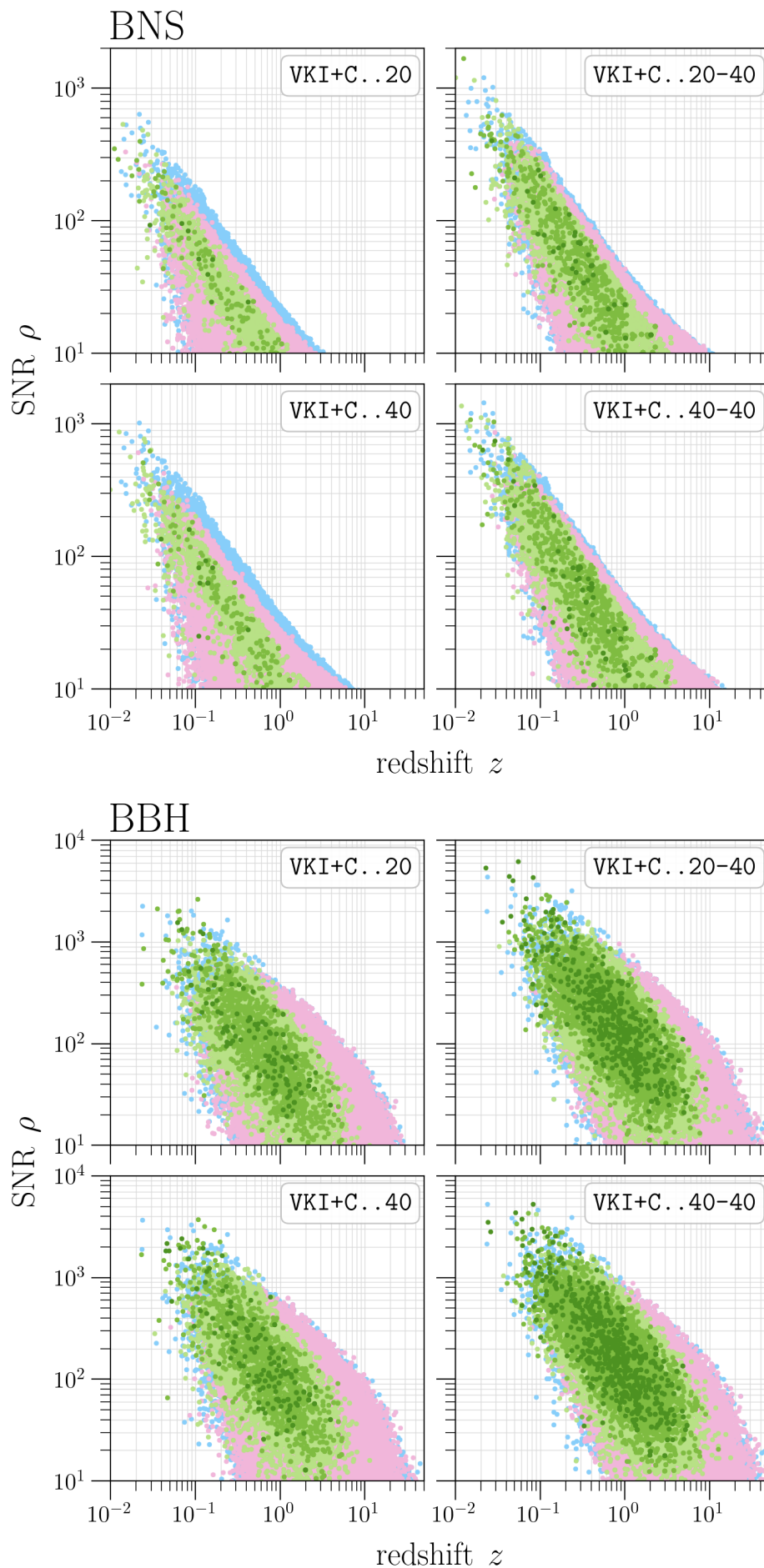


FIG. 18. The scatter plots illustrate the correlations between redshift z , SNR ρ , and 90%-credible sky area Ω_{90} for BNS (*top*) and BBH (*bottom*) mergers in the four studied CE networks. The blue dots indicate injections without Ω_{90} -information due ill-conditioned Fisher matrices. The plots were generated from injections corresponding to an observation time of **10 years**.

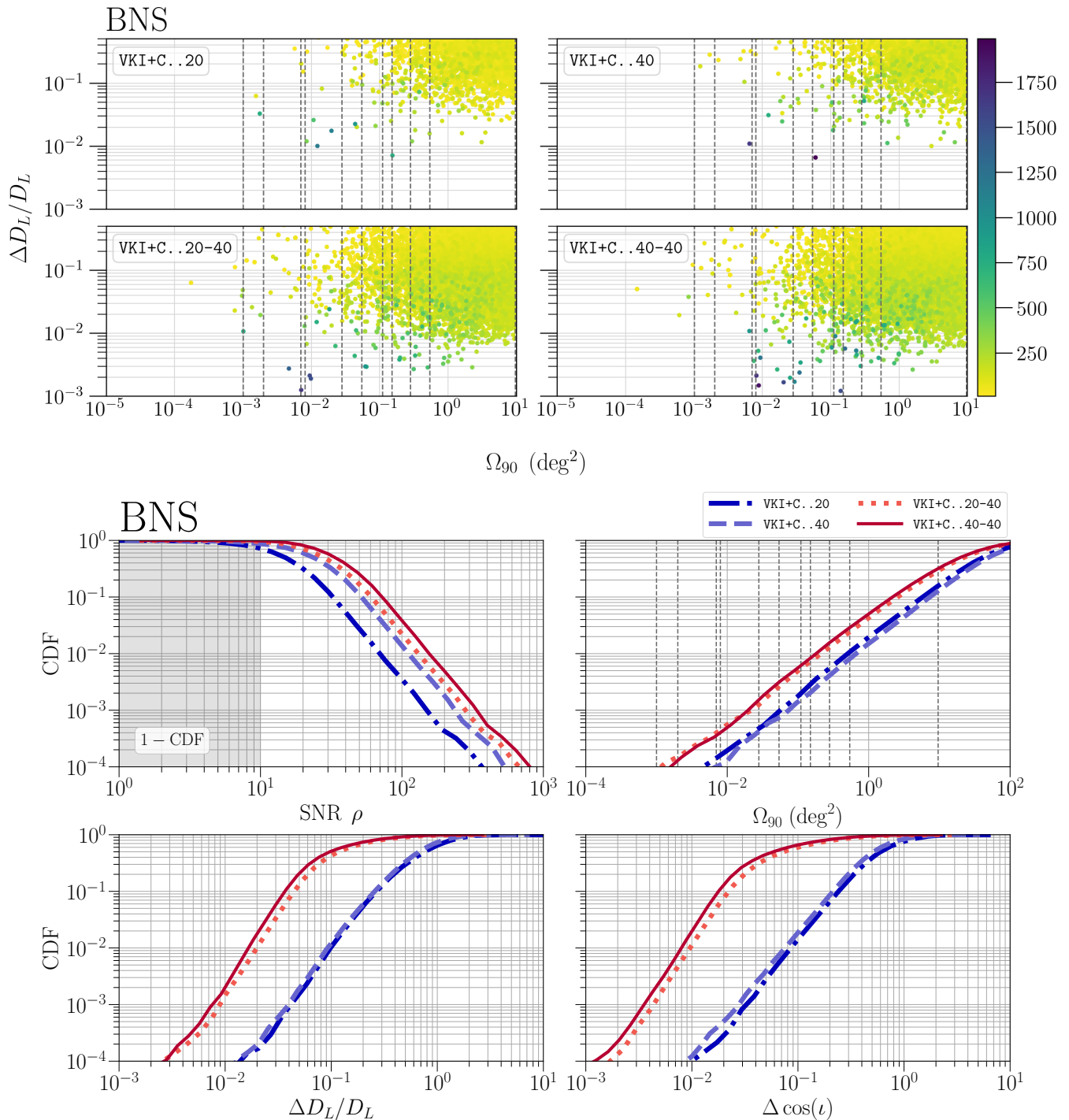


FIG. 19. *Top:* The scatter plots illustrate the correlations between SNR ρ , 90%-credible sky area Ω_{90} , and fractional luminosity distance error $\Delta D_L/D_L$ for BNS mergers with SNR $\rho \geq 10$ in the four studied CE networks for redshifts $z \leq 0.5$. The color bar indicates the SNR of the events. The plots were generated from injections corresponding to an observation time of **10 years**.

Bottom: Cumulative density function (CDF) for the SNR ρ , 90%-credible sky area Ω_{90} , fractional luminosity distance errors $\Delta D_L/D_L$, and absolute errors on the cosine of the inclination angle $\Delta \cos(\iota)$ for BNS mergers observed in the four studied CE networks for redshifts $z \leq 0.5$. The non-SNR panels are obtained for events with SNR $\rho \geq 10$, indicated by the non-shaded region in the SNR panel. The SNR CDF is flipped to highlight the behavior for large values.

Both: The dashed vertical lines in the Ω_{90} panels indicate the FOVs of the EM telescopes specified in Tab. VI.

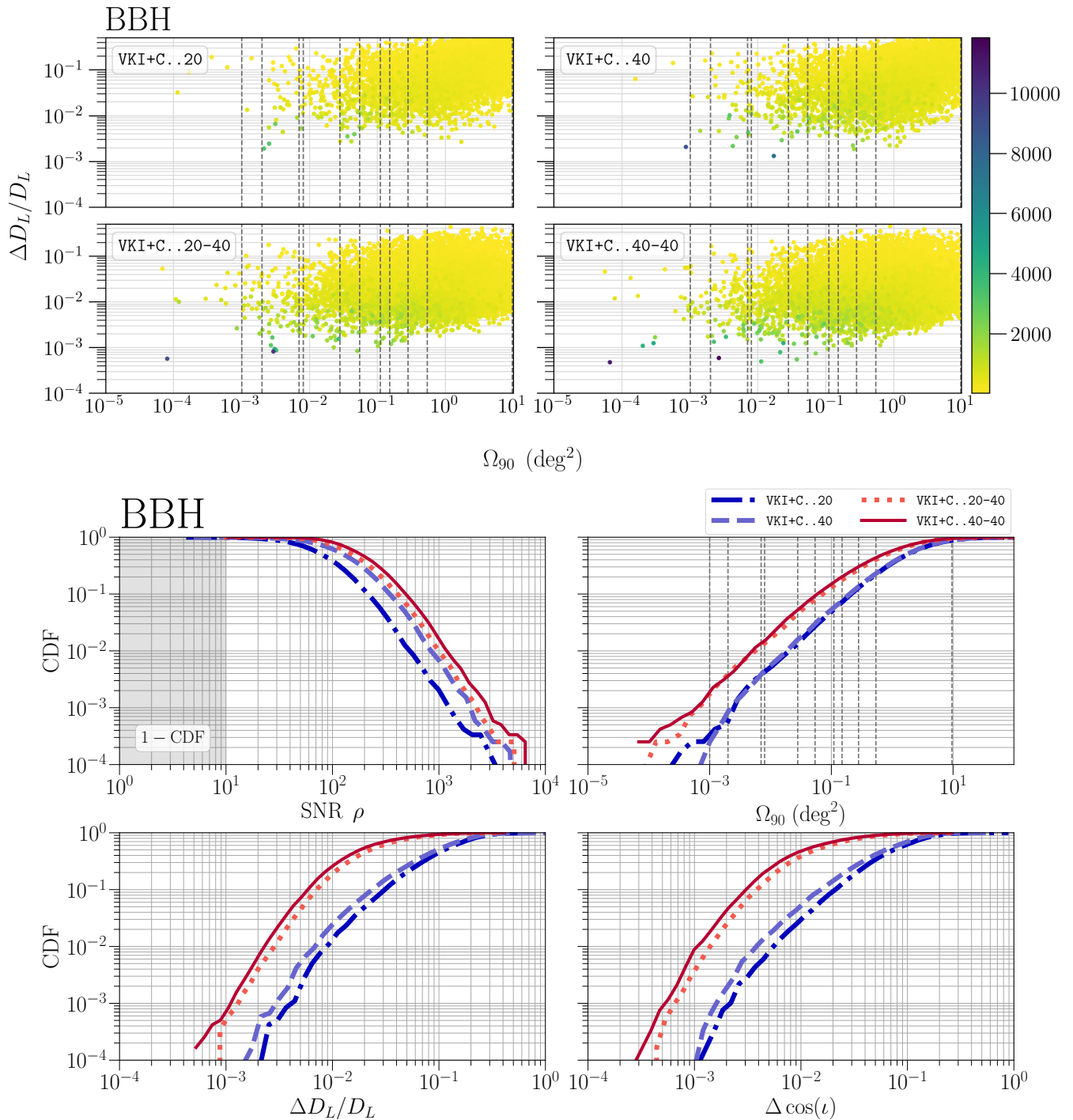


FIG. 20. *Top:* The scatter plots illustrate the correlations between SNR ρ , 90%-credible sky area Ω_{90} , and fractional luminosity distance error $\Delta D_L/D_L$ for BBH mergers with SNR $\rho \geq 10$ in the four studied CE networks for redshifts $z \leq 0.5$. The color bar indicates the SNR of the events. The plots were generated from injections corresponding to an observation time of **10 years**.

Bottom: Cumulative density function (CDF) for the SNR ρ , 90%-credible sky area Ω_{90} , fractional luminosity distance errors $\Delta D_L/D_L$, and absolute errors on the cosine of the inclination angle $\Delta \cos(\iota)$ for BBH mergers observed in the four studied CE networks for redshifts $z \leq 0.5$. The non-SNR panels are obtained for events with SNR $\rho \geq 10$, indicated by the non-shaded region in the SNR panel. The SNR CDF is flipped to highlight the behavior for large values.

Both: The dashed vertical lines in the Ω_{90} panels indicate the FOVs of the EM telescopes specified in Tab. VI.

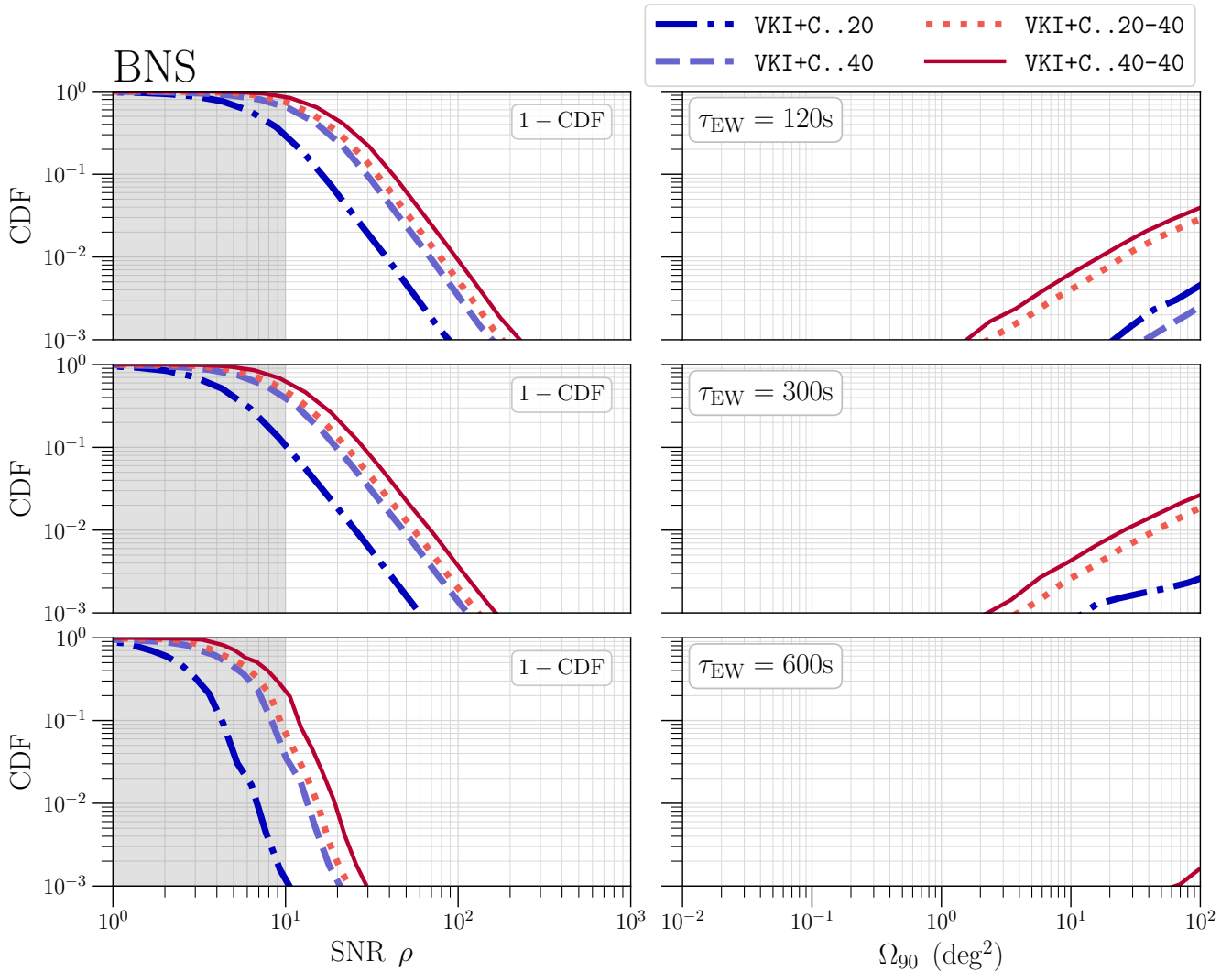


FIG. 21. The 3G networks will facilitate observation of the early onset of BNS mergers by a variety of different telescopes such as the Rubin observatory, EUCLID, WFIRST, Chandra x-ray observatory, 20 m Telescope, Keck II, VLT, ELT, GMT. The figure shows the cumulative histogram of the fraction of BNS events within a redshift of 0.5 as a function of SNR (left) and sky resolution (right) 2 minutes, 5 minutes and 10 minutes before merger. *[SSB: is this necessary?]* The 3G networks of KI+EC, and ECS will be able to detect $\geq 90\%$ of the events 2 minutes before merger localize 10% and 20% of all events within 10 deg². ET with A+ array of detectors can provide tens of events within the same localization but a single CE with the A+ will only provide a handful of early warning alerts.

TABLE IX. The best-fit parameters a , b , and c of the sigmoid function fitted to the efficiency $\epsilon(z, \rho_*)$ of detector networks in Fig. 2: $f(z) = [(1 + b)/(1 + b e^{az})]^c$ for two values of the SNR threshold $\rho_* = 10$ and $\rho_* = 100$.

Sigmoid parameter	$\rho_* = 10$			$\rho_* = 100$		
	a	b	c	a	b	c
<i>BNS</i>						
HLVKI+	62.08	0.005840	0.3341	607.7	0.006674	0.3529
VK+HLIv	30.03	0.0101	0.3082	306.2	0.01034	0.3124
HLKI+E	14.60	0.0070	0.1583	128.1	0.008706	0.2335
VKI+C	5.116	0.1201	0.1756	36.54	0.08155	0.4812
KI+EC	6.095	0.01788	0.1288	47.26	0.01737	0.34500
ECS	5.267	0.01060	0.08888	36.58	0.01405	0.3419
<i>BBH</i>						
HLVKI+	24.29	0.002173	0.08169	196.8	0.004368	0.11689
VK+HLIv	15.01	0.001851	0.04941	90.64	0.009464	0.1212
HLKI+E	14.20	0.00005143	0.007595	41.41	0.005331	0.0804
VKI+C	14.20	0.08272	0.002808	4.984	0.09012	0.1124
KI+EC	1.732	0.02680	0.01662	18.57	0.009260	0.07918
ECS	0.03980	0.09887	2.108	15.72	0.004978	0.06507

TABLE X. The best-fit parameters a , b , and c of the sigmoid function fitted to the efficiency $\epsilon(z, \rho_*)$ of detector networks in Fig. 13: $f(z) = [(1 + b)/(1 + b e^{az})]^c$ for two values of the SNR threshold $\rho_* = 10$ and $\rho_* = 100$.

Sigmoid parameter	$\rho_* = 10$			$\rho_* = 100$		
	a	b	c	a	b	c
<i>BNS</i>						
VKI+C. . 20	62.08	0.005840	0.3341	607.7	0.006674	0.3529
VKI+C. . 40	5.116	0.1201	0.1756	36.54	0.08155	0.4812
VKI+C. . 20-40	14.60	0.0070	0.1583	128.1	0.008706	0.2335
VKI+C. . 40-40	6.095	0.01788	0.1288	47.26	0.01737	0.34500
<i>BBH</i>						
VKI+C. . 20	24.29	0.002173	0.08169	196.8	0.004368	0.11689
VKI+C. . 40	14.20	0.08272	0.002808	4.984	0.09012	0.1124
VKI+C. . 20-40	15.01	0.001851	0.04941	90.64	0.009464	0.1212
VKI+C. . 40-40	14.20	0.00005143	0.007595	41.41	0.005331	0.0804

- [1] LIGO SCIENTIFIC collaboration, *Advanced LIGO*, *Class. Quant. Grav.* **32** (2015) 074001 [1411.4547].
- [2] VIRGO collaboration, *Advanced Virgo: a second-generation interferometric gravitational wave detector*, *Class. Quant. Grav.* **32** (2015) 024001 [1408.3978].
- [3] LIGO SCIENTIFIC, VIRGO collaboration, *Observation of Gravitational Waves from a Binary Black Hole Merger*, *Phys. Rev. Lett.* **116** (2016) 061102 [1602.03837].
- [4] LIGO SCIENTIFIC, VIRGO collaboration, *GW151226: Observation of Gravitational Waves from a 22-Solar-Mass Binary Black Hole Coalescence*, *Phys. Rev. Lett.* **116** (2016) 241103 [1606.04855].
- [5] LIGO SCIENTIFIC, VIRGO collaboration, *GW170104: Observation of a 50-Solar-Mass Binary Black Hole Coalescence at Redshift 0.2*, *Phys. Rev. Lett.* **118** (2017) 221101 [1706.01812].
- [6] LIGO SCIENTIFIC, VIRGO collaboration, *GWTC-1: A Gravitational-Wave Transient Catalog of Compact Binary Mergers Observed by LIGO and Virgo during the First and Second Observing Runs*, *Phys. Rev.* **X9** (2019) 031040 [1811.12907].
- [7] LIGO SCIENTIFIC, VIRGO collaboration, *GWTC-2: Compact Binary Coalescences Observed by LIGO and Virgo During the First Half of the Third Observing Run*, [2010.14527].
- [8] LIGO SCIENTIFIC, VIRGO collaboration, *GW170817: Observation of Gravitational Waves from a Binary Neutron Star Inspiral*, *Phys. Rev. Lett.* **119** (2017) 161101 [1710.05832].
- [9] LIGO SCIENTIFIC, VIRGO collaboration, *GW190425: Observation of a Compact Binary Coalescence with Total Mass $\sim 3.4M_{\odot}$* , *Astrophys. J. Lett.* **892** (2020) L3 [2001.01761].
- [10] LIGO SCIENTIFIC, VIRGO, FERMI GBM, INTEGRAL, IceCUBE, ASTROSAT CADMIUM ZINC TELLURIDE IMAGER TEAM, IPN, INSIGHT-HXMT, ANTARES, SWIFT, AGILE TEAM, 1M2H TEAM, DARK ENERGY CAMERA GW-EM, DES, DLT40, GRAWITA, FERMI-LAT, ATCA, ASKAP, LAS CUMBRES OBSERVATORY GROUP, OZGRAV, DWF (DEEPER WIDER FASTER PROGRAM), AST3, CAASTRO, VINROUGE, MASTER, J-GEM, GROWTH, JAGWAR, CALTECHNRAO, TTU-NRAO, NuSTAR, PAN-STARRS, MAXI TEAM, TZAC CONSORTIUM, KU, NORDIC OPTICAL TELESCOPE, ePESSTO, GROND, TEXAS TECH UNIVERSITY, SALT GROUP, TOROS, BOOTES, MWA, CALET, IKI-GW FOLLOW-UP, H.E.S.S., LOFAR, LWA, HAWC, PIERRE AUGER, ALMA, EURO VLBI TEAM, PI OF SKY, CHANDRA TEAM AT MCGILL UNIVERSITY, DFN, ATLAS TELESCOPES, HIGH TIME RESOLUTION UNIVERSE SURVEY, RIMAS, RATIR, SKA SOUTH AFRICA/MEERKAT collaboration, *Multi-messenger Observations of a Binary Neutron Star Merger*, *Astrophys. J. Lett.* **848** (2017) L12 [1710.05833].
- [11] LIGO SCIENTIFIC, VIRGO, FERMI-GBM, INTEGRAL collaboration, *Gravitational Waves and Gamma-rays from a Binary Neutron Star Merger: GW170817 and GRB 170817A*, *Astrophys. J. Lett.* **848** (2017) L13 [1710.05834].
- [12] K. Chatziioannou et al., *On the properties of the massive binary black hole merger GW170729*, *Phys. Rev.* **D100** (2019) 104015 [1903.06742].
- [13] LIGO SCIENTIFIC, VIRGO collaboration, *GW190521: A Binary Black Hole Merger with a Total Mass of $150M_{\odot}$* , *Phys. Rev. Lett.* **125** (2020) 101102 [2009.01075].
- [14] LIGO SCIENTIFIC, VIRGO collaboration, *Properties and Astrophysical Implications of the $150 M_{\odot}$ Binary Black Hole Merger GW190521*, *Astrophys. J. Lett.* **900** (2020) L13 [2009.01190].
- [15] LIGO SCIENTIFIC, VIRGO collaboration, *GW190412: Observation of a Binary-Black-Hole Coalescence with Asymmetric Masses*, *Phys. Rev.* **D102** (2020) 043015 [2004.08342].
- [16] LIGO SCIENTIFIC, VIRGO collaboration, *GW190814: Gravitational Waves from the Coalescence of a 23 Solar Mass Black Hole with a 2.6 Solar Mass Compact Object*, *Astrophys. J. Lett.* **896** (2020) L44 [2006.12611].
- [17] LIGO SCIENTIFIC, VIRGO collaboration, *Tests of general relativity with GW150914*, *Phys. Rev. Lett.* **116** (2016) 221101 [1602.03841].
- [18] N. Yunes, K. Yagi and F. Pretorius, *Theoretical Physics Implications of the Binary Black-Hole Mergers GW150914 and GW151226*, *Phys. Rev.* **D94** (2016) 084002 [1603.08955].
- [19] LIGO SCIENTIFIC, VIRGO collaboration, *Tests of General Relativity with GW170817*, *Phys. Rev. Lett.* **123** (2019) 011102 [1811.00364].
- [20] K. Belczynski et al., *Evolutionary roads leading to low effective spins, high black hole masses, and O1/O2 rates for LIGO/Virgo binary black holes*, *Astron. Astrophys.* **636** (2020) A104 [1706.07053].
- [21] B. F. Schutz, *Determining the Hubble Constant from Gravitational Wave Observations*, *Nature* **323** (1986) 310.
- [22] LIGO SCIENTIFIC, VIRGO, 1M2H, DARK ENERGY CAMERA GW-E, DES, DLT40, LAS CUMBRES OBSERVATORY, VINROUGE, MASTER collaboration, *A gravitational-wave standard siren measurement of the Hubble constant*, *Nature* **551** (2017) 85 [1710.05835].
- [23] E. E. Flanagan and T. Hinderer, *Constraining neutron star tidal Love numbers with gravitational wave detectors*, *Phys. Rev.* **D77** (2008) 021502 [0709.1915].
- [24] S. De, D. Finstad, J. M. Lattimer, D. A. Brown, E. Berger and C. M. Biwer, *Tidal Deformabilities and Radii of Neutron Stars from the Observation of GW170817*, *Phys. Rev. Lett.* **121** (2018) 091102 [1804.08583].
- [25] LIGO SCIENTIFIC, VIRGO collaboration, *GW170817: Measurements of neutron star radii and equation of state*, *Phys. Rev. Lett.* **121** (2018) 161101 [1805.11581].
- [26] M. R. Drout et al., *Light Curves of the Neutron Star Merger GW170817/SSS17a: Implications for R-Process Nucleosynthesis*, *Science* **358** (2017) 1570 [1710.05443].
- [27] D. A. Coulter et al., *Swope Supernova Survey 2017a (SSS17a), the Optical Counterpart to a Gravitational Wave Source*, *Science* (2017) [1710.05452].
- [28] P. S. Cowperthwaite et al., *The Electromagnetic Counterpart of the Binary Neutron Star Merger LIGO/Virgo GW170817. II. UV, Optical, and Near-infrared Light Curves and Comparison to Kilonova Models*, *Astrophys. J. Lett.* **848** (2017) L17 [1710.05840].
- [29] D. Kasen, B. Metzger, J. Barnes, E. Quataert and E. Ramirez-Ruiz, *Origin of the heavy elements in binary neutron-star mergers from a gravitational wave event*, *Nature* (2017) [1710.05463].
- [30] DES, DARK ENERGY CAMERA GW-EM collaboration, *The Electromagnetic Counterpart of the Binary Neutron Star Merger LIGO/Virgo GW170817. I. Discovery of the Optical Counterpart Using the Dark Energy Camera*, *Astrophys. J. Lett.* **848** (2017) L16 [1710.05459].
- [31] S. Valenti, D. J. Sand, S. Yang, E. Cappellaro, L. Tartaglia, A. Corsi et al., *The discovery of the electromagnetic counterpart of GW170817: kilonova AT 2017gfo/HLT17ck*,

- Astrophys. J. Lett.* **848** (2017) L24 [1710.05854].
- [32] I. Arcavi et al., *Optical emission from a kilonova following a gravitational-wave-detected neutron-star merger*, *Nature* **551** (2017) 64 [1710.05843].
- [33] N. R. Tanvir et al., *The Emergence of a Lanthanide-Rich Kilonova Following the Merger of Two Neutron Stars*, *Astrophys. J. Lett.* **848** (2017) L27 [1710.05455].
- [34] V. M. Lipunov et al., *MASTER Optical Detection of the First LIGO/Virgo Neutron Star Binary Merger GW170817*, *Astrophys. J. Lett.* **850** (2017) L1 [1710.05461].
- [35] P. A. Evans et al., *Swift and NuSTAR observations of GW170817: detection of a blue kilonova*, *Science* **358** (2017) 1565 [1710.05437].
- [36] J. M. Ezquiaga and M. Zumalacárregui, *Dark Energy After GW170817: Dead Ends and the Road Ahead*, *Phys. Rev. Lett.* **119** (2017) 251304 [1710.05901].
- [37] B. Margalit and B. D. Metzger, *Constraining the Maximum Mass of Neutron Stars From Multi-Messenger Observations of GW170817*, *Astrophys. J. Lett.* **850** (2017) L19 [1710.05938].
- [38] M. Ruiz, S. L. Shapiro and A. Tsokaros, *GW170817, General Relativistic Magnetohydrodynamic Simulations, and the Neutron Star Maximum Mass*, *Phys. Rev. D* **97** (2018) 021501 [1711.00473].
- [39] E. R. Most, L. R. Weih, L. Rezzolla and J. Schaffner-Bielich, *New constraints on radii and tidal deformabilities of neutron stars from GW170817*, *Phys. Rev. Lett.* **120** (2018) 261103 [1803.00549].
- [40] M. Shibata, E. Zhou, K. Kiuchi and S. Fujibayashi, *Constraint on the maximum mass of neutron stars using GW170817 event*, *Phys. Rev. D* **100** (2019) 023015 [1905.03656].
- [41] D. A. Godzieba, D. Radice and S. Bernuzzi, *On the maximum mass of neutron stars and GW190814*, *Astrophys. J.* **908** (2021) 122 [2007.10999].
- [42] M. Sasaki, T. Suyama, T. Tanaka and S. Yokoyama, *Primordial Black Hole Scenario for the Gravitational-Wave Event GW150914*, *Phys. Rev. Lett.* **117** (2016) 061101 [1603.08338].
- [43] S. Bird, I. Cholis, J. B. Muñoz, Y. Ali-Haïmoud, M. Kamionkowski, E. D. Kovetz et al., *Did LIGO detect dark matter?*, *Phys. Rev. Lett.* **116** (2016) 201301 [1603.00464].
- [44] B. Carr, F. Kuhnel and M. Sandstad, *Primordial Black Holes as Dark Matter*, *Phys. Rev. D* **94** (2016) 083504 [1607.06077].
- [45] LIGO SCIENTIFIC, VIRGO collaboration, *GW150914: Implications for the stochastic gravitational wave background from binary black holes*, *Phys. Rev. Lett.* **116** (2016) 131102 [1602.03847].
- [46] T. Regimbau, M. Evans, N. Christensen, E. Katsavounidis, B. Sathyaprakash and S. Vitale, *Digging deeper: Observing primordial gravitational waves below the binary black hole produced stochastic background*, *Phys. Rev. Lett.* **118** (2017) 151105 [1611.08943].
- [47] LIGO SCIENTIFIC, VIRGO collaboration, *GW170817: Implications for the Stochastic Gravitational-Wave Background from Compact Binary Coalescences*, *Phys. Rev. Lett.* **120** (2018) 091101 [1710.05837].
- [48] KAGRA, LIGO SCIENTIFIC, VIRGO collaboration, *Prospects for Observing and Localizing Gravitational-Wave Transients with Advanced LIGO, Advanced Virgo and KAGRA*, *Living Rev. Rel.* **21** (2018) 3 [1304.0670].
- [49] D. Reitze et al., *Cosmic Explorer: The U.S. Contribution to Gravitational-Wave Astronomy beyond LIGO*, *Bull. Am. Astron. Soc.* **51** (2019) 035 [1907.04833].
- [50] KAGRA collaboration, *KAGRA: 2.5 Generation Interferometric Gravitational Wave Detector*, *Nature Astron.* **3** (2019) 35 [1811.08079].
- [51] KAGRA collaboration, *Overview of KAGRA: Detector design and construction history*, [2005.05574].
- [52] A. G. Riess, S. Casertano, W. Yuan, L. M. Macri and D. Scolnic, *Large Magellanic Cloud Cepheid Standards Provide a 1% Foundation for the Determination of the Hubble Constant and Stronger Evidence for Physics beyond Λ CDM*, *Astrophys. J.* **876** (2019) 85 [1903.07603].
- [53] H.-Y. Chen, M. Fishbach and D. E. Holz, *A two per cent Hubble constant measurement from standard sirens within five years*, *Nature* **562** (2018) 545 [1712.06531].
- [54] S. Borhanian, A. Dhani, A. Gupta, K. G. Arun and B. S. Sathyaprakash, *Dark Sirens to Resolve the Hubble–Lemaître Tension*, *Astrophys. J. Lett.* **905** (2020) L28 [2007.02883].
- [55] LIGO collaboration, *A cryogenic silicon interferometer for gravitational-wave detection*, *Class. Quant. Grav.* **37** (2020) 165003 [2001.11173].
- [56] M. Punturo et al., *The Einstein Telescope: A third-generation gravitational wave observatory*, *Class. Quant. Grav.* **27** (2010) 194002.
- [57] S. Hild et al., *Sensitivity Studies for Third-Generation Gravitational Wave Observatories*, *Class. Quant. Grav.* **28** (2011) 094013 [1012.0908].
- [58] LIGO SCIENTIFIC collaboration, *Exploring the Sensitivity of Next Generation Gravitational Wave Detectors*, *Class. Quant. Grav.* **34** (2017) 044001 [1607.08697].
- [59] K. Ackley et al., *Neutron Star Extreme Matter Observatory: A kilohertz-band gravitational-wave detector in the global network*, *Publ. Astron. Soc. Austral.* **37** (2020) e047 [2007.03128].
- [60] B. S. Sathyaprakash, B. F. Schutz and C. Van Den Broeck, *Cosmography with the Einstein Telescope*, *Class. Quant. Grav.* **27** (2010) 215006 [0906.4151].
- [61] M. Punturo et al., *The third generation of gravitational wave observatories and their science reach*, *Class. Quant. Grav.* **27** (2010) 084007.
- [62] W. Zhao, C. Van Den Broeck, D. Baskaran and T. G. F. Li, *Determination of Dark Energy by the Einstein Telescope: Comparing with CMB, BAO and SNIa Observations*, *Phys. Rev. D* **83** (2011) 023005 [1009.0206].
- [63] B. Sathyaprakash et al., *Scientific Objectives of Einstein Telescope*, *Class. Quant. Grav.* **29** (2012) 124013 [1206.0331].
- [64] S. Vitale and M. Evans, *Parameter estimation for binary black holes with networks of third generation gravitational-wave detectors*, *Phys. Rev. D* **95** (2017) 064052 [1610.06917].
- [65] S. Vitale and C. Whittle, *Characterization of binary black holes by heterogeneous gravitational-wave networks*, *Phys. Rev. D* **98** (2018) 024029 [1804.07866].
- [66] R. X. Adhikari et al., *Astrophysical science metrics for next-generation gravitational-wave detectors*, *Class. Quant. Grav.* **36** (2019) 245010 [1905.02842].
- [67] E. D. Hall and M. Evans, *Metrics for next-generation gravitational-wave detectors*, *Class. Quant. Grav.* **36** (2019) 225002 [1902.09485].
- [68] B. S. Sathyaprakash et al., *Cosmology and the Early Universe*, [1903.09260].
- [69] B. S. Sathyaprakash et al., *Multimessenger Universe with Gravitational Waves from Binaries*, [1903.09277].
- [70] B. S. Sathyaprakash et al., *Extreme Gravity and Fundamental Physics*, [1903.09221].
- [71] V. Kalogera et al., *Deeper, Wider, Sharper: Next-Generation Ground-Based Gravitational-Wave Observations of Binary Black Holes*, [1903.09220].
- [72] M. Maggiore et al., *Science Case for the Einstein Telescope*, *JCAP* **03** (2020) 050 [1912.02622].

- [73] LIGO SCIENTIFIC, VIRGO collaboration, *Population Properties of Compact Objects from the Second LIGO-Virgo Gravitational-Wave Transient Catalog*, [2010.14533].
- [74] C. Cutler and E. E. Flanagan, *Gravitational waves from merging compact binaries: How accurately can one extract the binary's parameters from the inspiral wave form?*, *Phys. Rev. D* **49** (1994) 2658 [gr-qc/9402014].
- [75] E. Poisson and C. M. Will, *Gravitational waves from inspiraling compact binaries: Parameter estimation using second postNewtonian wave forms*, *Phys. Rev. D* **52** (1995) 848 [gr-qc/9502040].
- [76] R. Balasubramanian, B. Sathyaprakash and S. Dhurandhar, *Gravitational waves from coalescing binaries: Detection strategies and Monte Carlo estimation of parameters*, *Phys. Rev. D* **53** (1996) 3033 [gr-qc/9508011].
- [77] S. Borhanian, *gwbench: a novel Fisher information package for gravitational-wave benchmarking*, [2010.15202].
- [78] L. S. Collaboration et al., *Lsc algorithm library suite*, (2020), <https://doi.org/10.7935/GT1W-FZ16>.
- [79] T. Dietrich, A. Samajdar, S. Khan, N. K. Johnson-McDaniel, R. Dudi and W. Tichy, *Improving the NRTidal model for binary neutron star systems*, *Phys. Rev. D* **100** (2019) 044003 [1905.06011].
- [80] L. London, S. Khan, E. Fauchon-Jones, C. García, M. Hannam, S. Husa et al., *First higher-multipole model of gravitational waves from spinning and coalescing black-hole binaries*, *Phys. Rev. Lett.* **120** (2018) 161102 [1708.00404].
- [81] B. S. Sathyaprakash and B. F. Schutz, *Physics, Astrophysics and Cosmology with Gravitational Waves*, *Living Rev. Rel.* **12** (2009) 2 [0903.0338].
- [82] L. Blanchet, *Gravitational Radiation from Post-Newtonian Sources and Inspiralling Compact Binaries*, *Living Rev. Rel.* **17** (2014) 2 [1310.1528].
- [83] K. Belczynski, D. E. Holz, T. Bulik and R. O'Shaughnessy, *The first gravitational-wave source from the isolated evolution of two 40-100 Msun stars*, *Nature* **534** (2016) 512 [1602.04531].
- [84] K. K. Y. Ng, S. Vitale, W. M. Farr and C. L. Rodriguez, *Probing multiple populations of compact binaries with third-generation gravitational-wave detectors*, [2012.09876].
- [85] W. Israel, *Event horizons in static vacuum space-times*, *Phys. Rev.* **164** (1967) 1776.
- [86] B. Carter, *Axisymmetric Black Hole Has Only Two Degrees of Freedom*, *Phys. Rev. Lett.* **26** (1971) 331.
- [87] O. Dreyer, B. J. Kelly, B. Krishnan, L. S. Finn, D. Garrison and R. Lopez-Aleman, *Black hole spectroscopy: Testing general relativity through gravitational wave observations*, *Class. Quant. Grav.* **21** (2004) 787 [gr-qc/0309007].
- [88] E. Berti, J. Cardoso, V. Cardoso and M. Cavaglia, *Matched-filtering and parameter estimation of ringdown waveforms*, *Phys. Rev. D* **76** (2007) 104044 [0707.1202].
- [89] S. Gossan, J. Veitch and B. S. Sathyaprakash, *Bayesian model selection for testing the no-hair theorem with black hole ringdowns*, *Phys. Rev. D* **85** (2012) 124056 [1111.5819].
- [90] I. Kamaretsos, M. Hannam, S. Husa and B. S. Sathyaprakash, *Black-hole hair loss: learning about binary progenitors from ringdown signals*, *Phys. Rev. D* **85** (2012) 024018 [1107.0854].
- [91] I. Kamaretsos, M. Hannam and B. Sathyaprakash, *Is black-hole ringdown a memory of its progenitor?*, *Phys. Rev. Lett.* **109** (2012) 141102 [1207.0399].
- [92] L. London, D. Shoemaker and J. Healy, *Modeling ringdown: Beyond the fundamental quasinormal modes*, *Phys. Rev. D* **90** (2014) 124032 [1404.3197].
- [93] S. Dhanpal, A. Ghosh, A. K. Mehta, P. Ajith and B. S. Sathyaprakash, *A no-hair test for binary black holes*, *Phys. Rev. D* **99** (2019) 104056 [1804.03297].
- [94] T. Islam, A. K. Mehta, A. Ghosh, V. Varma, P. Ajith and B. S. Sathyaprakash, *Testing the no-hair nature of binary black holes using the consistency of multipolar gravitational radiation*, *Phys. Rev. D* **101** (2020) 024032 [1910.14259].
- [95] J. M. Lattimer, *Equation of State from Neutron Star Mass and Radius Measurements*, *JPS Conf. Proc.* **31** (2020) 011021.
- [96] T. Hinderer, B. D. Lackey, R. N. Lang and J. S. Read, *Tidal deformability of neutron stars with realistic equations of state and their gravitational wave signatures in binary inspiral*, *Phys. Rev. D* **81** (2010) 123016 [0911.3535].
- [97] T. Damour, A. Nagar and L. Villain, *Measurability of the tidal polarizability of neutron stars in late-inspiral gravitational-wave signals*, *Phys. Rev. D* **85** (2012) 123007 [1203.4352].
- [98] W. Kastaun and F. Ohme, *Finite tidal effects in GW170817: Observational evidence or model assumptions?*, *Phys. Rev. D* **100** (2019) 103023 [1909.12718].
- [99] D. A. Godzieba, R. Gamba, D. Radice and S. Bernuzzi, *Updated universal relations for tidal deformabilities of neutron stars from phenomenological equations of state*, [2012.12151].
- [100] R. Smith, S. Borhanian, B. Sathyaprakash, F. H. Vivanco, S. Field, P. Lasky et al., "Bayesian inference for gravitational waves from binary neutron star mergers in third-generation observatories." 2010.
- [101] K. Takami, L. Rezzolla and L. Baiotti, *Constraining the Equation of State of Neutron Stars from Binary Mergers*, *Phys. Rev. Lett.* **113** (2014) 091104 [1403.5672].
- [102] S. Bose, K. Chakravarti, L. Rezzolla, B. S. Sathyaprakash and K. Takami, *Neutron-star Radius from a Population of Binary Neutron Star Mergers*, *Phys. Rev. Lett.* **120** (2018) 031102 [1705.10850].
- [103] M. Breschi, S. Bernuzzi, F. Zappa, M. Agathos, A. Perego, D. Radice et al., *kiloHertz gravitational waves from binary neutron star remnants: time-domain model and constraints on extreme matter*, *Phys. Rev. D* **100** (2019) 104029 [1908.11418].
- [104] P. J. Easter, S. Ghonge, P. D. Lasky, A. R. Casey, J. A. Clark, F. H. Vivanco et al., *Detection and parameter estimation of binary neutron star merger remnants*, *Phys. Rev. D* **102** (2020) 043011 [2006.04396].
- [105] M. Shibata, K. Taniguchi and K. Uryu, *Merger of binary neutron stars with realistic equations of state in full general relativity*, *Phys. Rev. D* **71** (2005) 084021 [gr-qc/0503119].
- [106] M. Shibata, K. Taniguchi and K. Uryu, *Merger of binary neutron stars of unequal mass in full general relativity*, *Phys. Rev. D* **68** (2003) 084020 [gr-qc/0310030].
- [107] M. Prakash, J. R. Cooke and J. M. Lattimer, *Quark - hadron phase transition in protoneutron stars*, *Phys. Rev. D* **52** (1995) 661.
- [108] E. R. Most, L. J. Papenfort, V. Dexheimer, M. Hanauske, S. Schramm, H. Stöcker et al., *Signatures of quark-hadron phase transitions in general-relativistic neutron-star mergers*, *Phys. Rev. Lett.* **122** (2019) 061101 [1807.03684].
- [109] S. Blacker, N.-U. F. Bastian, A. Bauswein, D. B. Blaschke, T. Fischer, M. Oertel et al., *Constraining the onset density of the hadron-quark phase transition with gravitational-wave observations*, *Phys. Rev. D* **102** (2020) 123023 [2006.03789].
- [110] C. M. Will, *The Confrontation between General Relativity and Experiment*, *Living Rev. Rel.* **17** (2014) 4 [1403.7377].
- [111] E. Berti et al., *Testing General Relativity with Present and Future Astrophysical Observations*, *Class. Quant. Grav.* **32** (2015) 243001 [1501.07274].
- [112] N. Yunes and X. Siemens, *Gravitational-Wave Tests of General Relativity with Ground-Based Detectors and Pulsar*

- Timing-Arrays*, *Living Rev. Rel.* **16** (2013) 9 [1304.3473].
- [113] W. G. Unruh and R. M. Wald, *Information Loss*, *Rept. Prog. Phys.* **80** (2017) 092002 [1703.02140].
- [114] S. W. Hawking, *Breakdown of Predictability in Gravitational Collapse*, *Phys. Rev. D* **14** (1976) 2460.
- [115] SUPERNOVA SEARCH TEAM collaboration, *Observational evidence from supernovae for an accelerating universe and a cosmological constant*, *Astron. J.* **116** (1998) 1009 [astro-ph/9805201].
- [116] SUPERNOVA COSMOLOGY PROJECT collaboration, *Measurements of Ω and Λ from 42 high redshift supernovae*, *Astrophys. J.* **517** (1999) 565 [astro-ph/9812133].
- [117] S. W. Hawking and R. Penrose, *The Singularities of gravitational collapse and cosmology*, *Proc. Roy. Soc. Lond. A* **314** (1970) 529.
- [118] S. E. Perkins, N. Yunes and E. Berti, *Probing Fundamental Physics with Gravitational Waves: The Next Generation*, *Phys. Rev. D* **103** (2021) 044024 [2010.09010].
- [119] A. Ghosh et al., *Testing general relativity using golden black-hole binaries*, *Phys. Rev. D* **94** (2016) 021101 [1602.02453].
- [120] A. Ghosh, N. K. Johnson-Mcdaniel, A. Ghosh, C. K. Mishra, P. Ajith, W. Del Pozzo et al., *Testing general relativity using gravitational wave signals from the inspiral, merger and ringdown of binary black holes*, *Class. Quant. Grav.* **35** (2018) 014002 [1704.06784].
- [121] M. Abernathy et al., *Einstein Gravitational-Wave Telescope: Conceptual Design Study*. Available at: https://tds.virgo-gw.eu/?call_file=ET-0106C-10.pdf, (2010).
- [122] X. Zhang, J. Yu, T. Liu, W. Zhao and A. Wang, *Testing Brans-Dicke gravity using the Einstein telescope*, *Phys. Rev. D* **95** (2017) 124008 [1703.09853].
- [123] K. G. Arun and C. M. Will, *Bounding the mass of the graviton with gravitational waves: Effect of higher harmonics in gravitational waveform templates*, *Class. Quant. Grav.* **26** (2009) 155002 [0904.1190].
- [124] A. Samajdar and K. G. Arun, *Projected constraints on the dispersion of gravitational waves using advanced ground- and space-based interferometers*, *Phys. Rev. D* **96** (2017) 104027 [1708.00671].